Master's Thesis

Study on Flexible Behavior of MOFs Having Different Functional Groups upon CO_2 Adsorption

Songho Lee

Department of Chemistry

Graduate School of UNIST

2018

Study on Flexible Behavior of MOFs Having Different Functional Groups upon CO_2 Adsorption

A thesis/dissertation
submitted to the Graduate School of UNIST
in partial fulfillment of the
requirements for the degree of
Master of Science

Songho Lee

07. 11. 2018 of submission

Approved by

Advisor
Hoi Ri Moon

Study on Flexible Behavior of MOFs Having Different Functional Groups upon CO_2 Adsorption

Songho Lee

This certifies that the thesis/dissertation of Songho Lee is approved.

07. 11. 2018

Advisor: Hoi Ri Moon

Wonyoung Choe

Sang Kyu Kwak

Abstract

Flexible metal-organic frameworks (MOFs) are considered as fascinating materials due to their unique characteristics which have dynamic pore system and reversible structural transition upon external stimuli. Many people have great interest of flexible MOF because these characteristics are rarely observed in other systems such as COFs (Covalent Organic Frameworks), and MOP (Metal Organic Polyhedra). One of the dynamic behavior, the flexibility, denoted as structure transformation by external stimuli such as light, guest molecule, heating, and pressure is originated from breathing, swelling, linker rotation, and subnetwork displacement. The flexibility causes frameworks to have dynamic behavior, which of MOFs is useful to gas storage, separation, and sensing applications in many fields because it is led by selective adsorption of specific molecules via host-guest interaction. Thus, rational design of flexible MOFs is very intriguing research to bring selectivity and specificity to MOFs. But, even if a lot of flexible MOFs have been developed for a long time, there are only a little case that flexibility could be fine-tuned by adjusting host-host interaction in changing various functional groups.

Most of all, in this work, we focused on studying for dynamic behavior called as "gate-opening" phenomena. To endow flexibility to frameworks, nickel-based macrocycle that can be rotating in accordance with evacuating guest-molecules is used. Also, using same macrocycle having arms of different functional groups, it was intended to control the flexibility, based on the fact that the macrocycle arms act as hinge. By using the four coordinative macrocycle, we construct the environment in which the ligand can be accessible only axial site, and as a result, it was easy to design 3D structure with arm of macrocycle oriented inside the pore. In addition, H_4BPTC which is four direction organic linker is used to make 3D structure. It gives flexibility to frameworks as it has many rotational sites.

Herein, five kinds of flexible MOFs, denoted as *flex*MOF(CH_3), *flex*MOF(CN)-I, *flex*MOF(CN)-II, *flex*MOF(CH_2), and *flex*MOF(OH), are successfully synthesized by using macrocycle containing four type of dangling functional groups and H_4BPTC ligand including many rotational sites. The self-assembly method was used to synthesize the single crystal, and not only the rate of diffusion but also the size of crystals could be controlled by adjusting the solubility. Those flexible MOFs show different sorption behaviors, gate-opening and breathing phenomenon, triggered by CO_2 molecules depending on the functional groups. To elucidate those different flexible behaviors, we analyzed the single-crystal diffraction (SCD) data and will calculate the rotational energies and interaction sites with regard to functional groups through computational simulations.

Contents

List of Figures

List of Tables

Nomenclatures

MOF	Metal-organic framework
MOP	Metal-organic polyhedron
ZIF	Zeolitic imidazolate framework
SCD	Single crystal x-ray diffraction
XRPD	X-ray powder diffraction
IR	Infrared
TGA	Thermogravimetric analysis
EA	Elemental analysis
BET	Brunauer-Emmett-Teller
DMF	*N,N*-dimethylformamide
DEF	*N,N*-diethylformamide
MeCN	Acetonitrile
H_4BPTC	[1,1'-biphenyl]-2,2',5,5'-tetracarboxylic acid
TEA	Triethylamine
NaOH	Sodium hydroxide
$HClO_4$	Perchloric acid
$NaClO_4$	Sodium perchlorate
$KMnO_4$	Potassium permanganate
KOH	Potassium hydroxide
CO_2	Carbon dioxide

I. Introduction

In the beginning of MOFs studies, many researchers had focused on making pore size large by using long organic linkers or improving the stability of MOFs to utilize various fields. In the case of 1st MOFs[1], the stability of MOF was always a considerable disadvantage in applying fields because structure breaks down when solvents are removed from pore. Researchers have started to focus on more robust MOFs research, called 2nd generation MOFs. It had been actively studied by numerous researchers for many years. In particular, Omar M.Yaghi had focused on a method called reticular synthesis[2], which use the suitable precursor to design the final structure to be targeted. In this way, the new MOFs with several types of stable and high porosity was developed, and it attracted great interest from many researchers. However, over the years, many people are interested in dynamic behavior of MOFs, for example, expansion/shrinkage of cell, gate-opening/closing, or reversible transition of structure. MOFs having dynamic behavior can be useful in various applications such as sensing, storage, separation, and drug delivery. Also, it has the advantage of being able to use working capacity by external stimuli more efficiently because structural transition occurs by external stimuli, which called as 3rd generation MOFs.

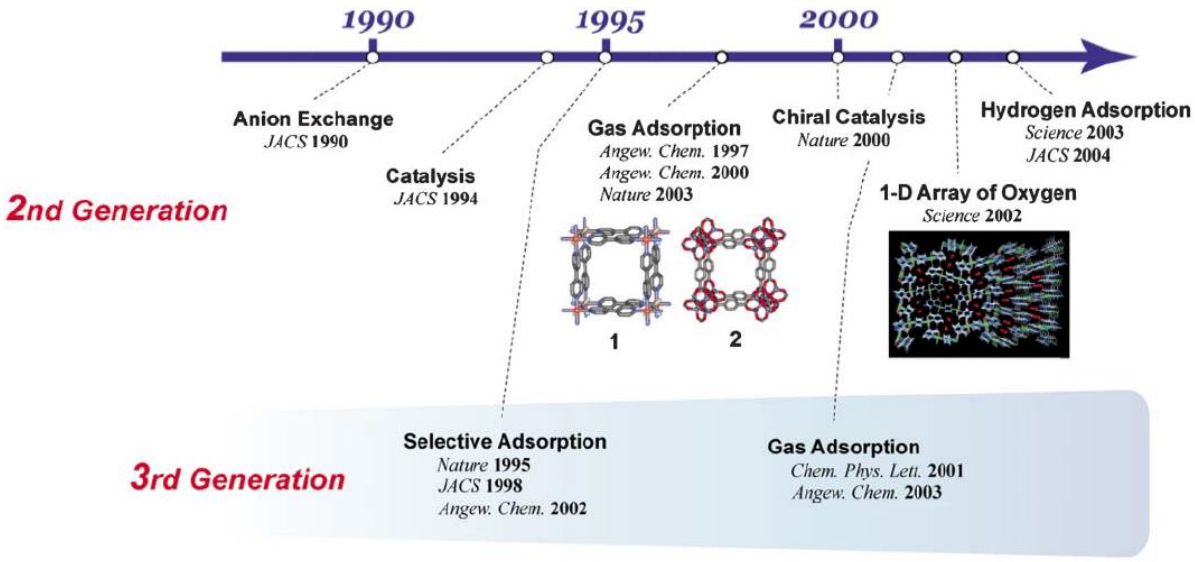

Figure 1.1. Overall history of MOF chemistry from 1900 to the present

Numerous flexible MOFs had been newly developed up to that time, but there had been rare on systematic and clear summary of the causes about the phenomenon. However, Kitagawa and Fischer made an effort to classify the cause or type of framework flexibility in order to establish the fundamental principles about framework flexibility in depth. Kitagawa[3] tried to sort out the terms that are commonly used in porous structures, and structural transformation of coordination polymer which has merit of

organic-inorganic hybrid material is categorized as the three types, that is recoverable collapsing, guest-induced transformation, and guest-induced reformation.

Also, the different modes of flexible MOFs were systematically classified into breathing, swelling, linker rotation, and subnetwork displacement by Fischer[4]. The flexibility is triggered or controlled by various crucial factors – functionalized organic linker[5], the type of metal clusters[6], linker rotation[7], angle between ligand and metal node[7], external stimuli (e.g. light[8], heat[9], mechanical pressure[10], guest[11]).

Most of all, the paper that flexibility can be tuned by functionalized organic linker was reported by Fischer's group. The frameworks of $[Zn_2(fu\text{-}bdc)_2(dabco)]_n$ could have characteristic of breathing behavior since the dangling chains could immobilize the guest molecules in pore as well as interact with framework backbone. The tendency was suggested in terms of the nine kinds of functionalized organic linker, and both the explanation for the tendency and the detailed experiment has become a significant precedent from the perspective of tuning the flexibility.

Also, according to whether polar solvent or non-polar solvent, continuous-breathing behavior is determined, and the mechanism of continuous breathing behavior is proposed by measuring SCD for each step[11]. The proposed mechanism is as follows (figure 1.2.). If polar solvent – DMF or H_2O – is present inside the pore, the structure is gradually contracted by host-guest interaction for the activation. This is because of intermolecular interaction with the framework and cation, particularly via hydrogen bonding or electrostatic interactions, which causes framework to undergo continuous breathing behavior.

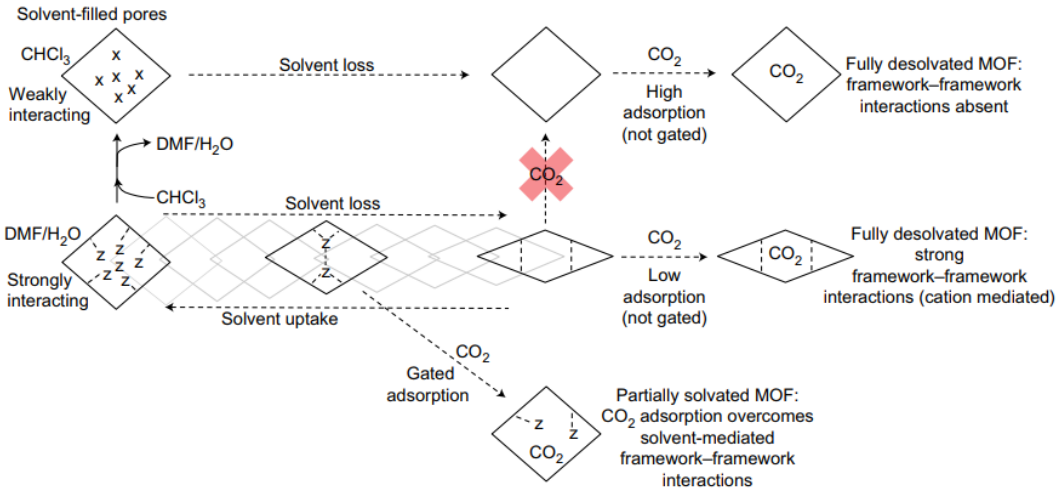

Figure 1.2. proposed role of guest-framework interactions

Although it has given the detailed description of the phenomenon as well as the deep understanding, it is still unclear how the certain factor affects flexibility of frameworks. This is because certain factor applies to flexibility of framework slightly at random. Therefore, rational fine-tuning the flexibility of MOFs is still challenging.

In previous study, a flexible MOF showing not only gate-opening behavior but also breathing phenomena had been designed. Through GCMC simulation, we could find the interaction site and type of interaction - van der Waals interaction occurring with the CO_2 molecules. It was found that the macrocycle arm, which act as hinge for the gate, has van der Waals interaction with CO_2. If the functional group of macrocycle arm, which act as hinge for the gate, can be substituted for another functional group, we anticipated that gate-opening behavior can be controlled by fine-tuning the frameworks. In this work, we focused on controlling for dynamic behavior called as “gate-opening” phenomena by introducing various functional groups – allyl, nitrile, hydroxyl, methyl.

II. Experimental Section

Materials and Methods. All chemicals and solvents used in the synthesis were of reagent grade and were used without further purification. 2,2'5,5'- teteramethylbiphenyl, 98% was bought from Alfa Aesar, and then 1,1'-biphenyl-2,2'5,5'-teteracarboxylic acid (H_4BPTC) was synthesized according to the reported paper. Distilled Acetonitrile was activated by distillation with P_2O_5 in an Ar atmosphere. The data of Thermogravimetric analysis (TGA) was measured at ramping rate 5 ºC / min under N_2(g) atmosphere using Q50 from TA instruments. Infrared spectra were measured on a Thermo Fisher Scientific Nicolet 6700 FT-IR spectrometer. XRPD data were collected using a Bruker D2 PHASER automated diffractometer at 30 kV and 10 mA for Cu Kα (λ = 1.54050 Å), with a step size of 0.02º in 2θ. The gas sorption data were collected by using a BELsorp-MAX, and PCTpro E&E - 122. UV/Vis diffuse reflectance spectra were recorded with a Cary 5000 UV/Vis spectrophotometer. Elemental analysis was conducted by UNIST Central Research Facilities center (UCRF) in Ulsan National Institute of Science and Technology (UNIST).

II.1. Macrocycle Synthesis

$[Ni(C_{12}H_{30}N_6O_2)](ClO^-_4)_2$, $NiL_{OH}(ClO^-_4)_2$. $NiL_{OH}(ClO^-_4)_2$ was synthesized on the basis of previously paper[12]. To a stirred methanol solution (50 mL) of $NiCl_2 \cdot 6H_2O$ (11.9 g) were slowly added ethylenediamine (6.8 mL) at 0 ºC, and then paraformaldehyde (7.5 g), ethanolamine (8.7 mL) was added in ordered refered. The residual mixture was sufficiently stirred at room temperature for about 30 min. Then, it was refluxed for 6 h. After it was cool down at r.t., the mixture was filtered, and purple powder was washed with MeOH, and dried at room temperature under vacuum. It was dissolved in deionized water 250 mL with stirring, and then 70% perchloric acid 10 mL was slowly added to yellow solution at 0 ºC. In addition, to provide excess anion, after $NaClO^-_4$ (2.6 g) was added, store it at refrigerator for 1 day. Then, yellow powder was formed, which were filtered off, washed with MeOH, and dried under vacuum. Yield : 17%. the yellow powder was recrystallized by using at least H_2O in heating water bath at 100 ºC, then crystal grows as it cool down, filtered it, washed MeOH, and dried at room temperature under vacuum. Anal. Calcd for $NiC_{12}H_{30}N_6O_8Cl_2$: C, 26.30; H, 5.52; N, 15.33.; Found : C, 26.15; H, 5.40; N, 15.49. FT-IR for $[NiL_{OH}](ClO^-_4)_2$ (ATR) : υ_{O-H} 3572, $\upsilon_{N-H(secondary\ amine)}$ 3205, υ_{C-H} 2985, 2891, υ_{ClO4} 1060 cm^{-1}.

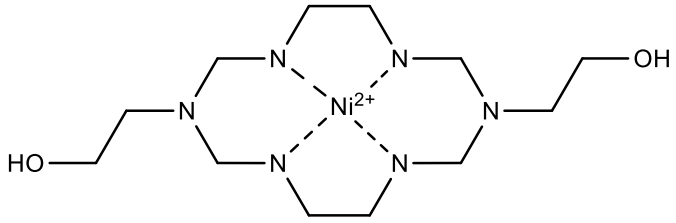

Figure 2.1.1. Nickel-based macrocyclic complex, $[NiL_{OH}](ClO^{-}_{4})_2$

$[Ni(C_{14}H_{30}N_6)](ClO^{-}_{4})_2$, $NiL_{CH2}(ClO^{-}_{4})_2$. $NiL_{CH2}(ClO^{-}_{4})_2$ was synthesized on the basis of previously paper[5], too. In the methanol solution (50 mL), $NiCl_2 \cdot 6H_2O$ (11.9 g, 0.05 mol) were stirred under ice bath condition, and then ethylenediamine (7.0 mL, 0.1 mol), paraformaldehyde (7.5 g, 0.25 mol), and allyllamine (8.4 mL, 0.11mol) was added in sequence refered. The residual mixture was sufficiently stirred at room temperature for about 30 min. Then, it was refluxed for 12 h. After it was cool down at r.t., the mixture was filtered, and pale purple powder was washed with MeOH, and dried at room temperature under vacuum. It was dissolved in deionized water 250 mL with stirring, and then 70% perchloric acid 10 mL was slowly added to yellow solution at 0 ºC. In addition, to provide excess anion, after $NaClO^{-}_{4}$ (2.6 g) was added, store it at refrigerator for 1 day. Then, yellow powder was formed, which were filtered off, washed with MeOH, and dried under vacuum. Yield : 8.6%. the yellow powder was recrystallized by using at least H_2O/MeCN = 1:1 (v/v) in heating water bath at 100 ºC, then crystal grows as it cool down, filtered it, washed MeOH, and dried at room temperature under vacuum. Anal. Calcd for $NiC_{14}H_{30}N_6O_8Cl_2$: C, 31.13; H, 5.60; N, 15.56.; Found : C, 31.05; H, 5.98; N, 16.75. FT-IR for $[NiL_{Allyl}](ClO^{-}_{4})_2$ (ATR) : $\upsilon_{C=C}$ 1639, $\upsilon_{N\text{-}H(secondary\ amine)}$ 3201, $\upsilon_{C\text{-}H}$ 2965, 2891, υ_{ClO4} 1068 cm^{-1}.

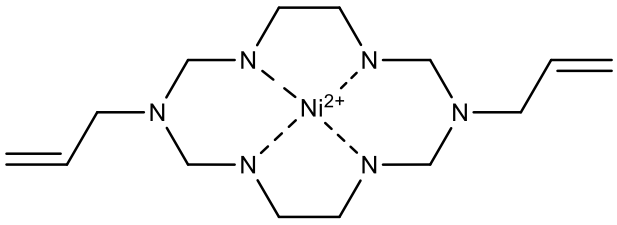

Figure 2.1.2. Nickel-based macrocyclic complex, $[NiL_{Allyl}](ClO^{-}_{4})_2$

$[Ni(C_{14}H_{28}N_8)](Cl^-_2)$, $NiL_{CN}(Cl^-_2)$. $NiL_{CN}(Cl^-_2)$ was synthesized like the preceding[4]. To a stirred methanol solution (50 mL) of $NiCl_2 \cdot 6H_2O$ (11.9 g, 0.05 mol) were slowly added ethylenediamine (6.8 mL, 0.1 mol) at 0 ºC, and then paraformaldehyde (7.5 g, 0.25 mol), 3-aminopropaneitrile (10 mL, 0.14mol) was added in ordered refered. The residual mixture was sufficiently stirred at room temperature for about 30 min. Then, it was refluxed for 24 h. After it was cool down at r.t., the mixture was filtered, and pale purple powder was washed with MeOH, and dried at room temperature under vacuum. The pale purple powder was recrystallized by using at MeOH 30 mL and at least H_2O in heating water bath at 100 ºC, then crystal grows as it cool down, filtered it, washed MeOH, and dried at room temperature under vacuum. Anal. Calcd for $NiC_{14}H_{28}N_8Cl_2$: C, 37.06; H, 6.80; N, 26.01.; Found : C, 38.38; H, 6.44; N, 25.58. FT-IR for $[NiL_{CN}](Cl^-)_2$ (ATR) : υ_{H2O} 3500 , $\upsilon_{C\equiv N}$ 2248 cm^{-1}, $\upsilon_{C\text{-}H}$ 2955, 2919 cm^{-1}.

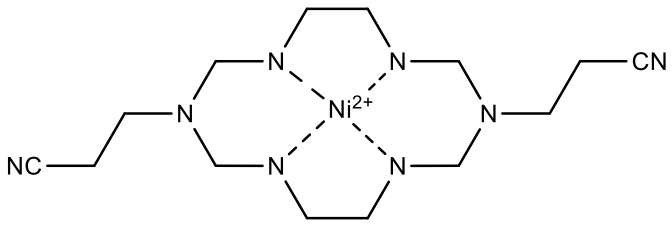

Figure 2.1.3. Nickel-based macrocyclic complex, $[NiL_{CN}](Cl_2)$

II.2. Ligand Synthesis

$C_{16}H_{10}O_8$, [1,1'-biphenyl]-2,2',5,5'-tetracarboxylic acid, H_4BPTC. $C_{16}H_{10}O_8$, H_4BPTC was synthesized on the basis of this paper[13]. After potassium permanganate (20 g) was mixed with water 100 mL, the mixture solution was heated at 100 ºC on the hot plate. It was sufficiently activated by heating for about 30 min, and then it was critical that it was slowly added to a heated solution of 2,2',5,5'-tetramthyl-1.1'-biphenyl 2 g in pyridine 20 mL for 90 min, still remains heating. And then, the reaction mixture was heated under reflux for 120 min. After heating, the reaction mixture was cooled down to room temperature, which filtered it by using gravity, washed with 0.3% aqueous KOH solution. The filterate was once more filtered out by using the membrane filter paper to seperate the manganese oxide of the smaller size particle. The diluted HCl, the concentrated hydrochloric acid : H_2O = 50 mL : 50 mL, was slowly added to the filterate. The white powder was precipitated, which stored at refrigerator for 1 day, filtered it, washed with D.I water. The white powder was dried at 60 ºC vacuum oven. Yield = 72% . 1H NMR (400 MHz, DMSO-d_6) 7.68 (s, 2H); 8.00 (m, 4H); 12.8 – 13.6 (bs, 4H). FT-IR for H_4BPTC (ATR) : $\upsilon_{C=O}$ 1678, $\upsilon_{carboxylic\ dimer}$ 2861, 2646, $\upsilon_{O\text{-}H}$ 3049 cm^{-1}.

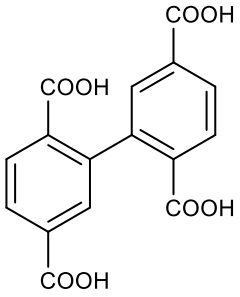

Figure 2.2.1. [1,1'-biphenyl]-2,2',5,5'-tetracarboxylic acid, H_4BPTC

II.3. Synthesis of Flexible MOFs through Self-Assembly Method

{[(NiL_{OH})$_2$BPTC]·1DMF·3H_2O}, *flex*-MOF(OH). [NiL_{OH}](ClO^-_4)$_2$ (64 mg, 0.014 mmol) was dissolved in H_2O 1.5 mL, DMF 1.5 mL by using ultra-sonication, which is layered in 10 mL vial. In another 10 mL vial, the mixture solution that H_4BPTC (24 mg, 0.07mmol) was dispersed in H_2O 2 mL, and then TEA(triethylamine) 80μL, DMF 1 mL was sequentially added was mixed with the macrocycle layer. The solution was shaking by the voltex mixer and stored at refrigerator for 3 days. Anal. Calcd for $Ni_2C_{43}H_{79}N_{13}O_{16}$: C, 44.85; H, 6.91; N, 15.81.; Found : C, 44.64; H, 6.94; N, 15.88. FT-IR for [NiL_{OH}]$_2$BTPC (ATR) : υ_{O-H} 3434, $\upsilon_{N-H(secondary\ amine)}$ 3154, υ_{C-H} 2926, 2869, υ_{COO-} 1571 , 1354 cm^{-1}.

{[(NiL_{CH2})$_2$BPTC]·1MeCN·5H_2O}, *flex*MOF(CH_2). [NiL_{CH2}](ClO^-_4)$_2$ (77.76 mg, 0.035 mmol) was dissolved in H_2O 1.0 mL, MeCN 2.0 mL by using ultra-sonication, which is layered in vial. In another vial, the mixture solution that H_4BPTC (23.6 mg, 0.07 mmol) was dispersed in H_2O 1 mL, and then TEA(triethylamine) 80μL, MeCN 2 mL was sequentially added was slowly layered on the macrocycle layer. Anal. Calcd for $Ni_2C_{46}H_{79}N_{13}O_{13}$: C, 48.48; H, 6.99; N, 15.98.; Found : C, 48.48; H, 6.24; N, 16.01. FT-IR for [NiL_{CH2}]$_2$BPTC(ATR): $\upsilon_{N-H(secondary\ amine)}$ 3139, υ_{C-H} 2914, 2862, υ_{COO-} 1571, 1343 cm^{-1}.

{[(NiL_{CN})$_2$BPTC]·4DMF·2H_2O}, *flex*MOF(CN)-I. [NiL_{CN}](Cl_2) (62 mg, 0.035 mmol) was dissolved in H_2O 1.5 mL, DMF 1.5 mL by using ultra-sonication. The remaining was filtered by using the syringe filter, which is layered in 10 mL vial. In another 10 mL vial, the mixture solution that H_4BPTC (24 mg, 0.07 mmol) was dispersed in H_2O 1 mL, and then TEA(triethylamine) 80μL, DMF 2

mL was sequentially added was shaking with the macrocycle layer by the voltex mixer and stored at refrigerator for 3 days. Anal. Calcd for $Ni_2C_{56}H_{94}N_{20}O_{14}$: C, 48.43; H, 6.82; N, 20.17.; Found : C, 48.44; H, 6.73; N, 20.10. FT-IR for $[NiL_{CN}]_2$BTPC (ATR) : υ_{CN} 2246, $\upsilon_{N\text{-}H(secondary\ amine)}$ 3154, $\upsilon_{C\text{-}H}$ 2926, 2869, $\upsilon_{COO\text{-}}$ 1572, 1381 cm^{-1}.

{[$(NiL_{CN})_2$BPTC]·4MeCN·5H_2O}, *flex*MOF(CN)-II. $[NiL_{CN}](Cl_2)$ (30.66 mg, 0.07 mmol) was dissolved in H_2O 0.7 mL and MeCN 1.8 mL solution by using ultra sonication. The macrocycle isn't totally dissolved in solution, but it doesn't matter. The mixture solution which has been melted to the maximum is placed on the bottom. H_4BPTC (11.48 mg, 0.035 mmol) was resolved in H_2O 0.3 mL, MeCN 2.2 mL, and triethylamine 80 μL. The ligand layer is stacked on the macrocycle layer by using Pasteur pipette and store it at room temperature for 3 days. Anal. Calcd for $Ni_2C_{52}H_{84}N_{20}O_{13}$: C, 47.50; H, 6.44; N, 21.31.; Found : C, 47.53; H, 6.28; N, 21.63. FT-IR for *flex*MOF(CN)-II (ATR) : υ_{CN} 2246, $\upsilon_{C\text{-}H}$ 2926, 2869, $\upsilon_{COO\text{-}}$ 1574, 1371 cm^{-1}.

Process of Exchange. All mother liquor of *as-flex*MOFs were washed with synthetic solvent condition of identical ratio to remove the unreacted molecules in solution, and then were exchanged with volatile solvent such as distilled MeCN and THF 6 times for 3 days. If crystals were exchanged without washing step, cracked crystals were observed with white powder. Crystallinity was so important to analyze the dried structure, so washing step is essential key step to keep crystal to be intact. In case of *flex*MOF(CH_2), *flex*MOF(CN)-I, *flex*MOF(CN)-II, crystals were exchanged with distilled MeCN 6 times for 3 days. In case of *flex*MOF(OH), crystals were exchanged with distilled THF in the same way as previous method.

II.4. Controlling Method of Synthetic Condition for Single Crystal

In this work, we tried to synthesize single crystal of flexible MOFs to analyze specific structures. This is because SCD is so vital tool in interpreting the structure obviously. As a result, five kinds of single crystal of flexible MOFs were successfully synthesized through self-assembly method at r.t or 10 °C. To synthesize single crystal in new solvent system, in advance, solubility test of macrocycle and ligand was processed by using general solvents, such as MeCN, MeOH, EtOH, H_2O, pyridine, Acetone, THF, DMF, DEF, DMSO, and DMA. Through the process, it is useful to control condition forming precipitations as well as to help each layer stack up layer-by-layer.

If solvent of low solubility was used excessively, precipitations of white powder occur immediately from the interface when stacking up the layer by using Pasteur pipette. In that case, three solutions exist to synthesize crystal. When the gel shaped-white precipitations are excessive, it is unlikely to form crystal because layer of thick precipitations obstructs diffusion between macrocycle layer and ligand. Firstly, to decrease the gel shaped-white precipitations, the solvent of the higher solubility has to be added in reaction condition. In this experiment, the solvent of the higher solubility was selected as H_2O, since H_2O was shown higher solubility to both macrocycle and H_4BPTC. The appropriate ratio between solvents is an important determinant of success. The reason why solubility test is important is because new reaction condition can be discovered with the extent that stacking by controlling amount of the gel shaped-white precipitations. Secondly, there is a way to get the crystal by lowering the concentration. This method is based on the fact that when there are less precursors in same amount of solvent, interaction between solvent and precursor can be stronger than before. I think that if difference of solubility is extreme, this method is not suitable as solution. Lastly, there is a way to get crystal with eliminating the gel type-precipitation at high temperature. But, please note that raising the temperature does not always prevent precipitation. This is because the solubility of each substance differs in accordance with temperature, in other words, there is a case that precipitation may occur well at high temperature. Among the three method, I think that first method is a fundamental solution to control solubility more easily.

On the contrary, if crystal is not formed because of rapidly diffusing between layers, there are three solutions, too. Generally, the growth of single crystal appears with diffusing molecules slowly for self-assembly, so controlling the rate of diffusion is important factor to form single crystal. The product can’t be precipitated by keeping melted form if fast diffusion occurs. First of all, the solvent of lower solubility was needed to put in reaction condition additionally so as to form crystal. Secondly, if the color of mixture solution was differently changed from previous one to the coordinated color, the concentration of each layer was increased. Lastly, there is a method of inducing crystallization by lowering the storage temperature. As mentioned earlier, this method does not always apply to all materials. This is because product may not always crystallize well at low temperature.

III. Results and Discussion

Single-Crystal X-ray crystallography

To obstruct losing crystallinity, paratone-*N* oil was used with single crystal since crystallinity decreased dynamically at exposing the air. The diffraction data was collected using ADSC Quantum-210 detector and PLSII-2D SMC at Pohang Accelerator Laboratory, Korea. All the data is analyzed by using the program called as The ADSC Q210 ADX program, HKL3000sm. Also, to solve the structure, SHELX-XT was used as direct methods, and the data was refined by full-matrix least-squares calculation. Both the data collection and processing was used for *RapidAuto* software. The structures were solved using direct methods with SHELX-XS and refined by full-matrix least-square calculation with SHELX-TL program package.

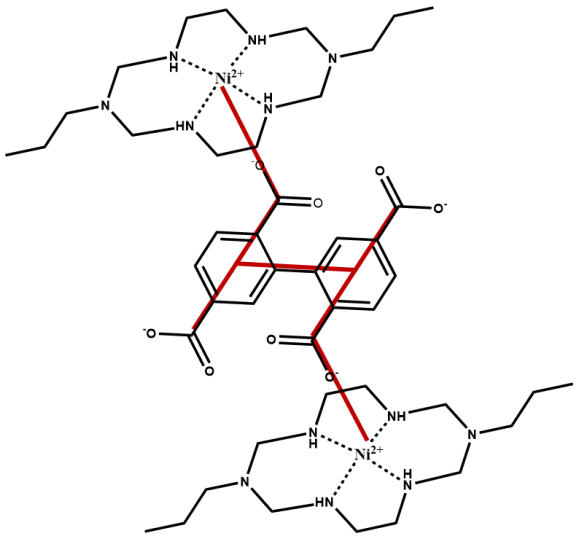

Figure 3. The simplifying method of *flex*MOFs, the structure of flexMOFs was simplified by using MS modeling program in order to see complicated structure easier than before. All the atoms were erased except for red line. The circle means nickel center of macrocycle, and the connected dimensions are represented by one color.

III. 1. *flex*-MOF(CN)-I

The single crystal can be obtained by controlling DMF:H_2O ratio through self-assembly method, which was analyzed through single crystal X-ray diffraction in Pohang Accelerator Laboratory. The

diffraction data were measured at 100 K, and were collected in two kinds of states as mother liquor and dried states. The functionalized arms of macrocycle is pointing inside the pore which is 3D structure. *as-flex*MOF(CN)-I was exchanged with distilled MeCN, followed by activation at 110 ºC for 4 h, and then *d-flex*MOF(CN)-I can be obtained. Through using SCD and MS modeling program, it was confirmed that the cell shrinks while changing from *as-flex*MOF to *d-flex*MOF, which was related with rotation of macrocycle. In the case of *flex*MOF(CN)-I, during drying process, it was confirmed that the new hydrogen bonds are formed with breaking the existing hydrogen bonds (figure 3.1.1.). As shown below, in the case of *flex*MOF(CN)-I, asymmetric unit is divided into two parts, Ni1A and Ni2B. In the case of Ni1A, there are four hydrogen bonds, and the positions of hydrogen bonding do not change during drying process, but the rotation of macrocyle occurs. On the other hand, in the case of Ni2B, the existing hydrogen bonding, pale green color (figure 3.1.1.a), was broken for drying process, and then new hydrogen bonding, pink color, was formed between N and O.

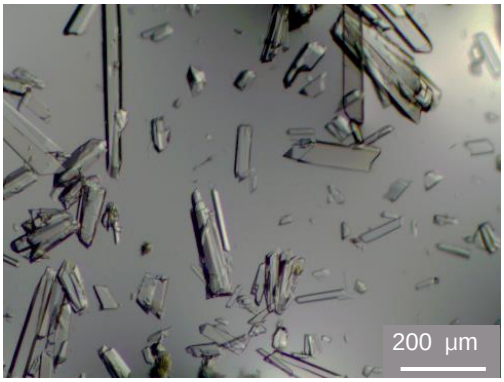

Figure 3.1.1. The microscope image of *flex*-MOF(CN)-I

(a)

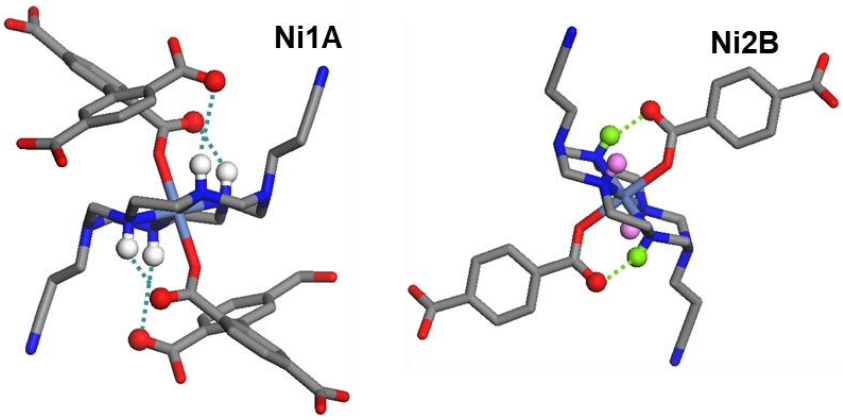

(b)

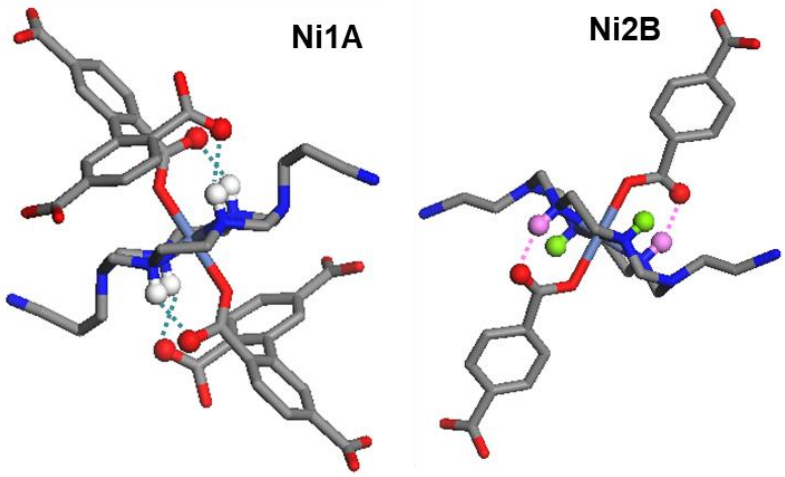

Figure 3.1.2. X-ray structure of *as-flex*MOF(CN)-I and *d-flex*MOF(CN)-I. (a) Asymmetric unit of *as-flex*MOF(CN)-I. Ni1A has four hydrogen bonding with secondary amine of macrocycle and carboxylate of BPTC. Ni2B has two hydrogen bonding with secondary amine of macrocycle and carboxylate of BPTC. (b) Asymmetric unit of *d-flex*MOF(CN)-I. Ni1A was observed that four hydrogen bonding still exist, but Ni2B was shown that different hydrogen bonding unlike previous bonding occur by rotating of macrocycle.

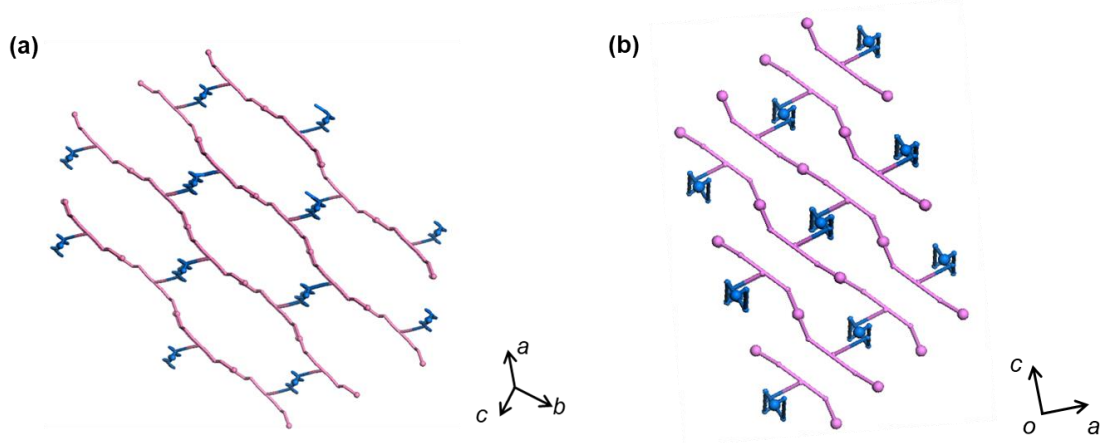

Figure 3.1.3. Simplified structure of *flex*MOF(CN)-I, figure 3.1.1 in the same way as previous method (a) simplified structure of *as-flex*MOF(CN)-I from the perspective of *abc* plane, (b) simplified structure of *d-flex*MOF(CN)-I from the perspective of *ac* plane.

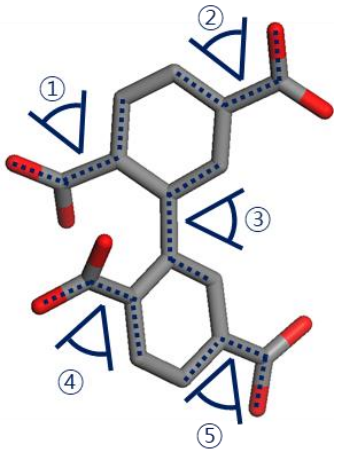

Figure 3.1.4. dihedral angle of *flex*MOF(CN)-I

Table 3.1.1. dihedral angle table of *flex*MOF(CN)-I

angle	*as-flex*MOF(CN)-I	*d-flex*MOF(CN)-I
①	-135.785º	-139.384º
②	-11.917º	169.276º
③	50.894º	59.833º
④	-135.785º	-118.301º
⑤	-11.917º	176.732º

As a result of comparing the dihedral angles of *as-flex*MOF(CN)-I, part ①, ④ and part ②, ⑤ appear identical angle (table 3.1.1.). But, the angle of d-flexMOF showed different tendency from that of as-flexMOF, and the greatest angle change was shown at part ②, ⑤.

Also, specific length was measured by using MS modeling program to determine the rectangular dimension through SCD analysis, as shown in figure 3.1.4, the rectangular dimension of *flex*MOF(CN)-I decreased from 21.57 × 25.48 $Å^2$ to 11.36 × 31.38 $Å^2$ after activation, (for *as-flex*MOF(CN)-I and *d-flex*MOF(CN)-I, respectively). This phenomena is that The rotation of macrocycle is caused to change the dihedral angle of BPTC, and result in shrinkage of the cell for activation.

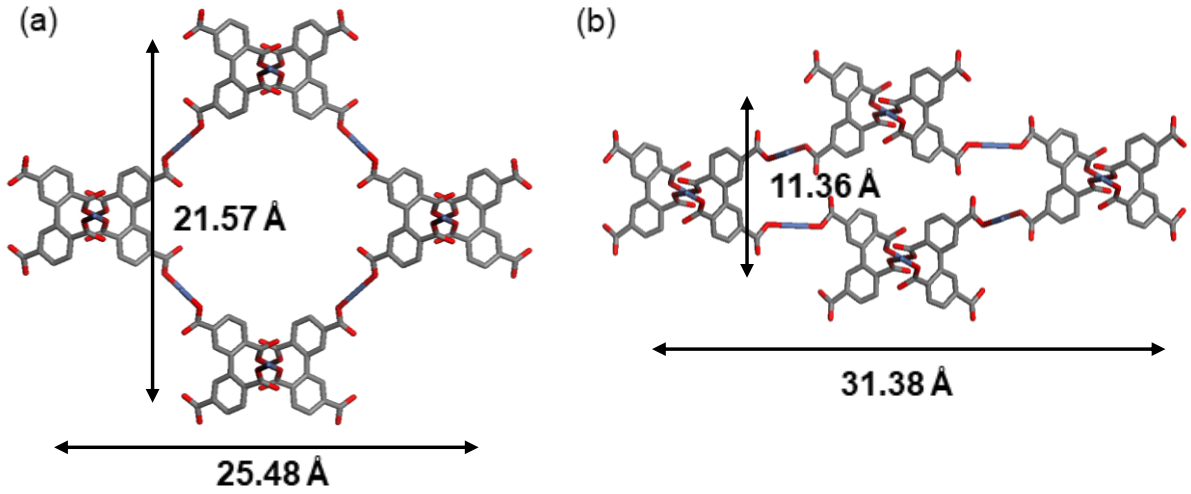

Figure 3.1.5. Cell shrinkage of *flex*MOF(CN)-I after activation observed using SCD

Table 3.1.2 X-ray crystallographic data of *as-flex*MOF(CN)-I

Compound	*as-flex*MOF(CN)-I
Formula	C22 H31 N8 Ni1 O4
crystal system	*Monoclinic*
space group	*C2/c*
Fw	530.26
a, Å	21.568(5)
b, Å	25.475(5)
c, Å	15.515(4)
α, deg	90
β, deg	93.143(11)
γ, deg	90
V, Å^3	8512(3)
Z	8
ρ_{calcd}, g cm^{-3}	0.828
temp , K	100
λ, Å	
μ, mm^{-1}	0.461
goodness-of-fit (F^2)	0.964
F(000)	2232
reflections collected	48415
independent reflections	14685 [R(int) = 0.1685]
completeness to θ_{max}, %	100.0
data/parameters/restraints	14685 / 0 / 319
θ range for data collection, deg	1.575 to 33.554
diffraction limits (*h*, *k*, *l*)	-33<=h<=33, -39<=k<=39, -23<=l<=23
refinement method	Full-matrix least-squares on F^2
R_1, wR_2 [I>2σ(I)]	0.0903, 0.2564
R_1, wR_2 (all data)	0.2409, 0.2893
largest peak, hole, eÅ^{-3}	0.497, -0.656

$^a R = \Sigma||F_o| - |F_c||/\Sigma|F_o|$. $^b wR(F^2) = [\Sigma w(F_o^2 - F_c^2)^2/\Sigma w(F_o^2)^2]^{1/2}$ where $w = 1/[\sigma^2(F_o^2) + (0.1048P)^2]$, $P = (F_o^2 + 2F_c^2)/3$.

Table 3.1.3. X-ray crystallographic data of *d-flex*MOF(CN)-I

Compound	*d-flex*MOF(CN)-I
Formula	C44 H62 N16 Ni2 O8
crystal system	*Triclinic*
space group	*P-1*
Fw	1060.51
a, Å	10.063(2)
b, Å	15.927(3)
c, Å	16.581(3)
α, deg	86.837(8)
β, deg	74.753(5)
γ, deg	78.205(9)
V, Å^3	2509.8(8)
Z	2
ρ_{calcd}, g cm^{-3}	1.403
temp , K	100
λ, Å	
μ, mm^{-1}	0.782
goodness-of-fit (F^2)	1.002
F(000)	1116
reflections collected	26462
independent reflections	14235[R(int) = 0.0927]
completeness to θ_{max}, %	93.3
data/parameters/restraints	14235 / 0 / 637
θ range for data collection, deg	1.795 to 32.853°
diffraction limits (*h*, *k*, *l*)	-14<=h<=14, -21<=k<=21, -23<=l<=23
refinement method	Full-matrix least-squares on F^2
R_1, wR_2 [$I>2\sigma(I)$]	R1 = 0.0985, wR2 = 0.2259
R_1, wR_2 (all data)	R1 = 0.2191, wR2 = 0.2788
largest peak, hole, eÅ^{-3}	0.671 and -0.833

[a] $R = \Sigma||F_o| - |F_c||/\Sigma|F_o|$. [b] $wR(F^2) = [\Sigma w(F_o^2 - F_c^2)^2/\Sigma w(F_o^2)^2]^{1/2}$ where $w = 1/[\sigma^2(F_o^2) + (0.1224P)^2]$, $P = (F_o^2 + 2F_c^2)/3$.

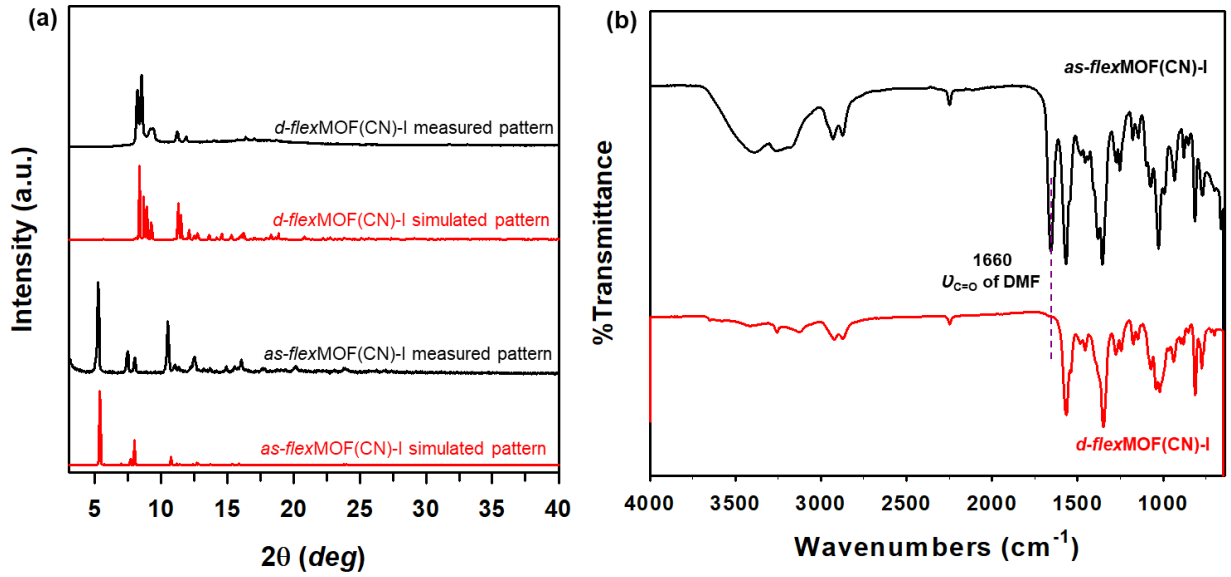

Figure 3.1.6. (a) XRPD patterns of *flex*MOF(CN)-I (Simulated pattern, red; as-synthesized compound, black), (b) IR spectrum of *as-flex*MOF(CN)-I and *d-flex*MOF(CN)-I

In figure 3.1.5. XRD data and Infra-red spectroscopy is for *as-flex*MOF(CN)-I and *d-flex*MOF(CN)-I, respectively. Both *as-flex*MOF(CN)-I and *d-flex*MOF(CN)-I is well matched with simulated pattern in XRD data. In the IR spectroscopic data, it was confirmed that the guest molecule, DMF, had been removed before and after the activation. Also, TGA and EA were simultaneously measured in same vial sample, and through the calculation, the number of solvents in the pores could be determined as $\{[(NiL_{CN})_2BPTC]\cdot 4DMF\cdot 2H_2O\}$ (figure 3.1.6.).

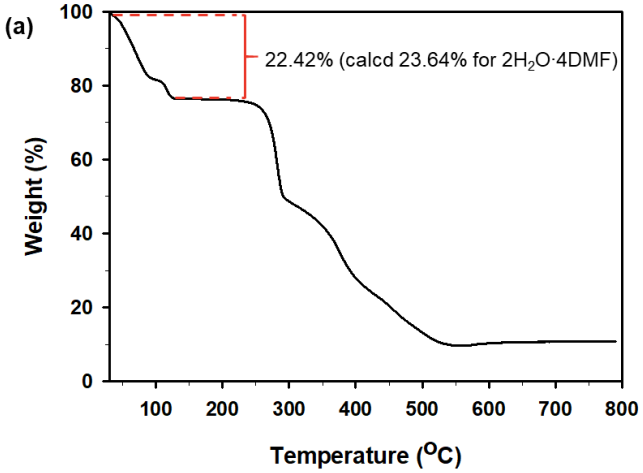

(b)

EA Results	1st	2nd	3rd	Calculated value
Carbon %	48.44	48.15	48.50	48.43
Hydrogen %	6.73	6.57	6.57	6.82
Nitrogen %	20.10	19.94	19.87	20.17
C/N ratio	2.81	2.82	2.85	2.80

Figure 3.1.7. (a) TGA trace of *as-flex*MOF(CN)-I, (b) Result of Elemental Analysis

Gas sorption property

To understand CO_2 sorption property, the low/high pressure sorption experiment were conducted, and sample preparation was done in the following way. *as-flex*MOF(CN)-I was sufficiently washed with DMF:H_2O = 3.5:2.5 (*v/v*) to remove the dissolved macrocycle and ligand, and then was exchanged with distilled MeCN 2 times a day in total for 6 times. The exchanged sample, *ex-flex*MOF(CN)-I, were introduced into the cell and activated at room temperature overnight under vacuum, followed by further 4 hours at 110 ºC under vacuum. Through the sorption experiment, it was confirmed that tendency of carbon dioxide sorption was changed according to activation condition (figure 3.7). When activated by the method of red graph, the steep adsorption of carbon dioxide was occurred at p / p_0 = 0.425. Meanwhile, in case of black graph activated by only RT under vacuum, two step adsorption curve was clearly observed. The result was considered the fact that the black graph was less activated than red one because black graph not only show less adsorption amount from red one but also different adsorption shape. Less adsorption amount means that the pore is filled by somethings such as guest molecules, but guest molecules isn't detected in IR spectrum because amount of molecules is too small to be detected in IR spectrum (figure 3.8). Also, two step adsorption is that the macrocycle is partially rotating over two steps because the pore is interrupted by something. Interestingly, in this work, carbon dioxide sorption property can be controlled in three ways, either by activating condition, by solvent system, or by metal clusters having various functional groups. These phenomenon were identically observed the same as the previous result at high pressure experiment. In case of only R.T activation, the sample was less activated than 110 ºC activation condition. In this case, the amount of adsorption is smaller than that of red one, and the adsorption shape of the graph is not steep like red one (figure 3.8). In both case, carbon dioxide wasn't entirely evacuated at the desorption part and the extent to which carbon dioxide was trapped can be controlled depending on activation conditions. *flex*MOF(CN)-I will be a commercially good candidate for trapping carbon dioxide.

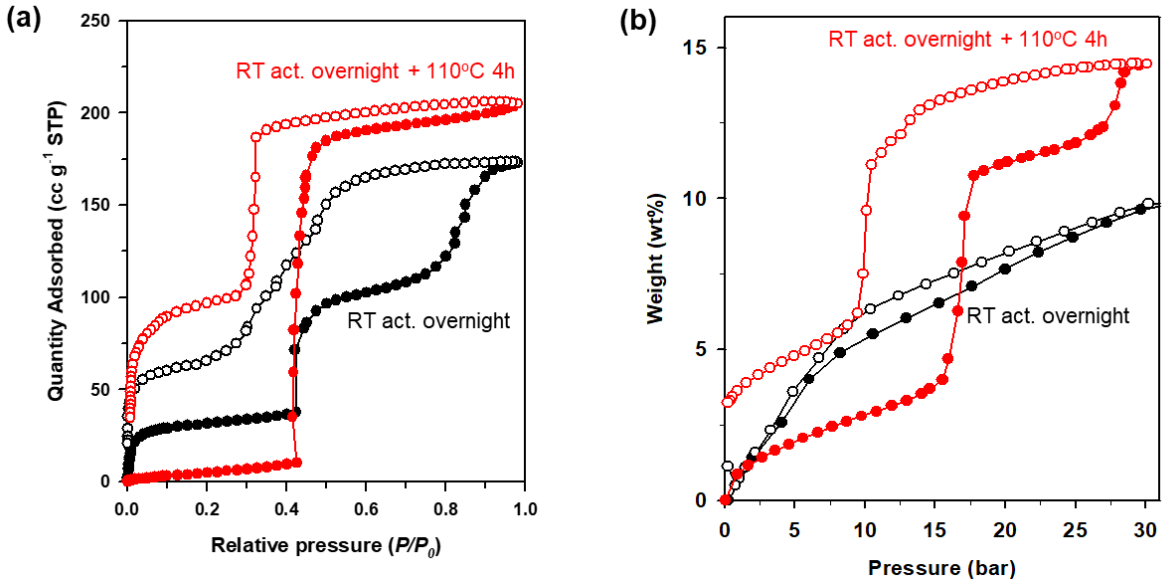

Figure 3.1.8. CO_2 sorption isotherm of *flex*MOF(CN)-I (a) Carbon dioxide sorption isotherms of *flex*MOF(CN)-I at low pressure and 196 K (R.T under vacuum overnight, black; R.T under vacuum overnight + 110°C for 4 h under vacuum, red (b) Carbon dioxide sorption isotherms at high pressure of *flex*MOF(CN)-I (R.T under vacuum overnight, black; R.T under vacuum overnight + 110°C for 4 h under vacuum, red)

III. 2. *flex*-MOF(CN)-II

The single crystal can be obtained by controlling MeCN:H_2O ratio through self-assembly method, which was analyzed through single crystal X-ray diffraction in Pohang Accelerator Laboratory. The diffraction data were collected at 100 K, and were measured in both mother liquor and dried states. Also, *as-flex*MOF(CN)-II was exchanged with distilled MeCN, followed by activation at room temperature overnight, and then *d-flex*MOF(CN)-I can be obtained. As a result of analyzing the SCD data before and after drying, cell shrinkage could be quantified specifically. Unlike *flex*MOF(CN)-I, in the case of *flex*MOF(CN)-II, the hydrogen bonds weren't broken and were maintained, but the rotation of the macrocycle still occur (figure 3.2.1.). Although the hydrogen bonds aren't newly formed, the rectangular dimension of *flex*MOF(CN)-II was changed from 16.77 × 28.17 $Å^2$ to 8.95 × 28.58 $Å^2$ (figure 3.2.4.). Later, these characteristic leads to different results in CO_2 gas adsorption experiments. There are four and two hydrogen bonds in the structure of *as-flex*MOF(CN)-II, and there exist the same number of hydrogen bonds in the structure of *d-flex*MOF(CN)-II. But, the macrocycle was still rotated, and the dihedral angle of BPTC also changed (figure 3.2.3.).

Figure 3.2.1. The microscope image of *flex*-MOF(CN)-II

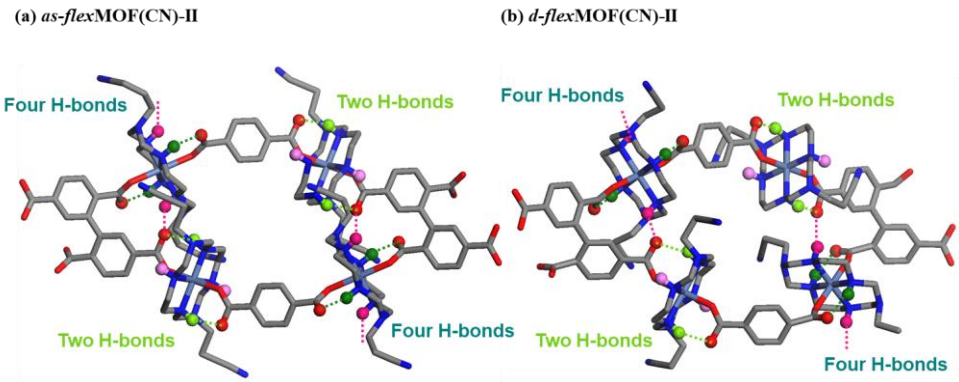

Figure 3.2.2. Comparison of hydrogen bonding for changing (a) *as-flex*MOF(CN)-II to (b) *d-flex*MOF(CN)-II.

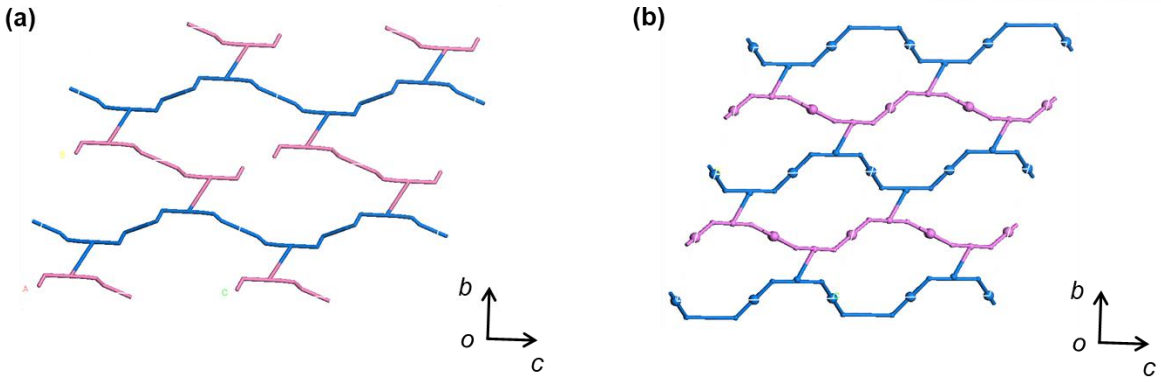

Figure 3.2.3. Simplified structure of *flex*MOF(CN)-II, figure 3 in the same way as previous method (a) simplified structure of *as-flex*MOF(CN)-II from the perspective of *bc* plane, (b) simplified structure of *d-flex*MOF(CN)-II from the perspective of b*c* plane.

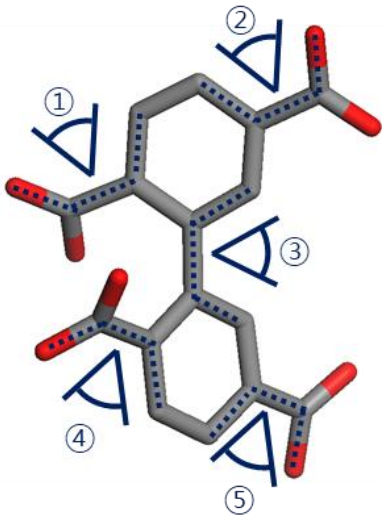

Figure 3.2.4. dihedral angle of *flex*MOF(CN)-II

Table 3.2.1. dihedral angle table of *flex*MOF(CN)-II

angle	*as-flex*MOF(CN)-II	*d-flex*MOF(CN)-II
①	65.825º	60.853º
②	-6.737º	1.576º
③	131.211º	136.326º
④	65.379º	97.516º
⑤	-6.317º	-21.514º

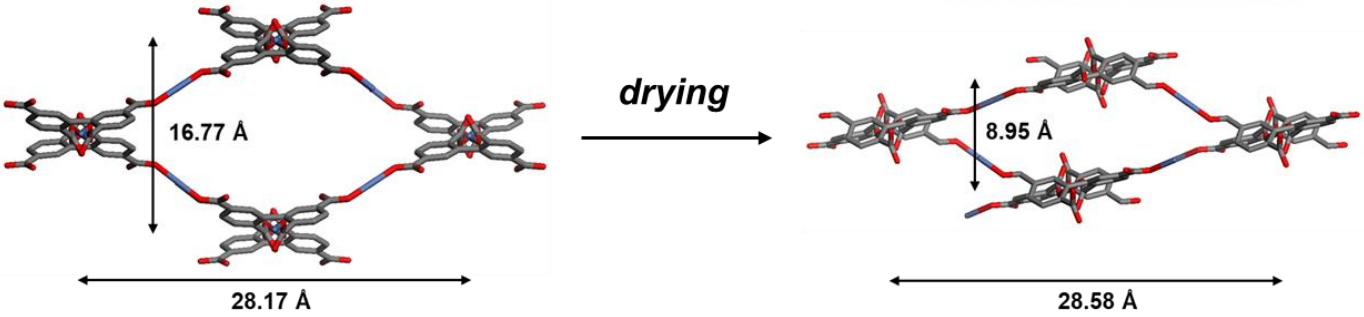

Figure 3.2.5. Change of cell size when activating *flex*MOF(CN)-II

Table 3.2.2. X-ray crystallographic data of *as-flex*MOF(CN)-II

Compound	*as-flex*MOF(CN)-II
Formula	C22 H31 N8 Ni1 O4
crystal system	*Monoclinic*
space group	*C2/c*
Fw	530.26
a, Å	21.568(5)
b, Å	25.475(5)
c, Å	15.515(4)
α, deg	90
β, deg	93.143(11)
γ, deg	90
V, Å^3	8512(3)
Z	8
ρ_{calcd}, g cm^{-3}	0.828
temp , K	100
λ, Å	
μ, mm^{-1}	0.461
goodness-of-fit (F^2)	0.964
F(000)	2232
reflections collected	48415
independent reflections	14685 [R(int) = 0.1685]
completeness to θ_{max}, %	100.0
data/parameters/restraints	14685 / 0 / 319
θ range for data collection, deg	1.575 to 33.554
diffraction limits (*h*, *k*, *l*)	-33<=h<=33, -39<=k<=39, -23<=l<=23
refinement method	Full-matrix least-squares on F^2
R_1, wR_2 [I>2σ(I)]	0.0903, 0.2564
R_1, wR_2 (all data)	0.2409, 0.2893
largest peak, hole, eÅ^{-3}	0.497, -0.656

$^a R = \Sigma||F_o| - |F_c||/\Sigma|F_o|$. $^b wR(F^2) = [\Sigma w(F_o^2 - F_c^2)^2/\Sigma w(F_o^2)^2]^{1/2}$ where $w = 1/[\sigma^2(F_o^2) + (0.2000P)^2]$, $P = (F_o^2 + 2F_c^2)/3$.

Table 3.2.3. X-ray crystallographic data of *d-flex*MOF(CN)-II

Compound	*d-flex*MOF(CN)-II
Formula	C44 H62 N16 Ni2 O8
crystal system	*Triclinic*
space group	*P-1*
Fw	1060.51
a, Å	8.954(4)
b, Å	16.093(5)
c, Å	18.683(7)
α, deg	69.66(2)
β, deg	79.159(10)
γ, deg	73.68(2)
V, Å^3	2410.4(16)
Z	2
ρ_{calcd}, g cm^{-3}	1.461
temp , K	100
λ, Å	
μ, mm^{-1}	0.814
goodness-of-fit (F^2)	0.939
F(000)	1116
reflections collected	26856
independent reflections	13857 [R(int) = 0.0568]
completeness to θ_{max}, %	91.6
data/parameters/restraints	13857 / 637 / 0
θ range for data collection, deg	2.044 to 33.267°
diffraction limits (*h*, *k*, *l*)	-12<=h<=12, -22<=k<=22, -29<=l<=28
refinement method	Full-matrix least-squares on F^2
R_1, wR_2 [$I>2\sigma(I)$]	0.0794, 0.2069
R_1, wR_2 (all data)	0.2267, 0.2667
largest peak, hole, eÅ^{-3}	0.626, -0.585

$^aR = \Sigma||F_o| - |F_c||/\Sigma|F_o|$. $^bwR(F^2) = [\Sigma w(F_o^2 - F_c^2)^2/\Sigma w(F_o^2)^2]^{1/2}$ where $w = 1/[\sigma^2(F_o^2) + (0.1230P)^2]$, $P = (F_o^2 + 2F_c^2)/3$.

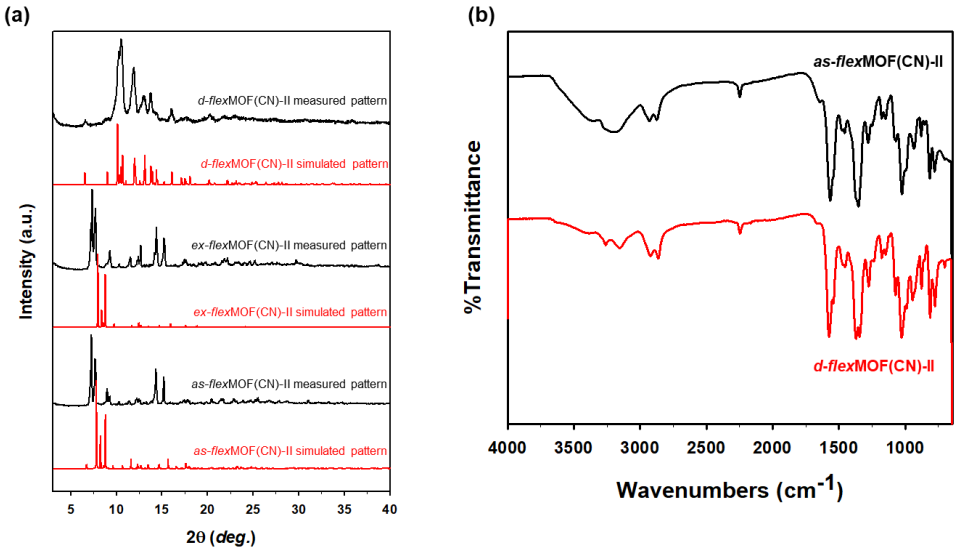

Figure 3.2.6. XRD graph and IR spectrum of *flex*MOF(CN)-II (a) Comparison of simulated pattern and measured pattern from *as-flex*MOF(CN)-II to *d-flex*MOF(CN)-II (simulated pattern, red; measured pattern, black) (b) IR spectrum of *flex*MOF(CN)-II

In figure 3.2.5. XRD data and Infra-red spectroscopy is for *as-flex*MOF(CN)-II and *d-flex*MOF(CN)-II, respectively. Both *as-flex*MOF(CN)-II and *d-flex*MOF(CN)-II is well matched with simulated pattern in XRD data. In the IR spectroscopic data, it was confirmed that the broad peak near 3200cm^{-1} disappeared after activation. It means that H_2O present in *as-flex*MOF(CN)-II was removed. In addition, it was confirmed that the coordination bond between metal and ligand was intact by keeping the carboxylate peak at 1650 cm^{-1}. TGA and EA were simultaneously measured in same vial sample, and through the calculation, the number of solvents in the pores could be determined as $\{[(NiL_{CN})_2BPTC]\cdot 4MeCN\cdot 5H_2O\}$ (figure 3.2.6.).

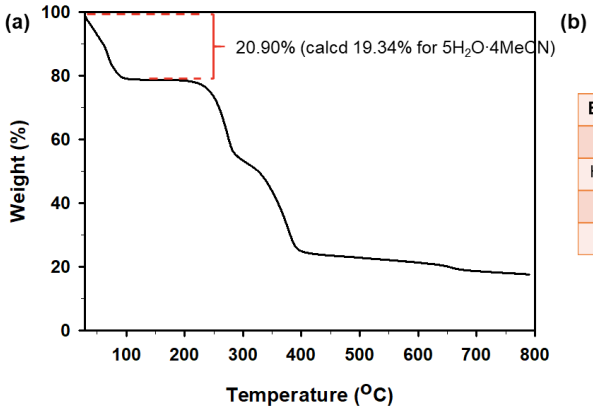

(b)

EA Results	1st	2nd	3rd	Calculated value
Carbon %	48.08	47.53	47.69	47.50
Hydrogen %	6.34	6.28	6.37	6.44
Nitrogen %	22.47	21.63	21.70	21.31
C/N ratio	2.50	2.56	2.56	2.59

Figure 3.2.7. (a) TGA trace of *as-flex*MOF(CN)-II, (b) Result of Elemental Analysis

Gas sorption property

To understand CO_2 sorption property, the low/high pressure sorption experiment were conducted, and sample preparation was done in the following way. *as-flex*MOF(CN)-II was sufficiently washed with MeCN:H_2O = 4:1 (v/v) to remove the unreacted macrocycle and ligand, and then was exchanged with distilled MeCN 2 times a day in total for 6 times. the exchanged sample, *ex-flex*MOF(CN)-II, were introduced into the cell and activated at room temperature overnight under vacuum. In control experiment of activation condition, it was experimentally confirmed that increasing the temperature leads to loss of crystallinity and decrease in adsorption amount. Therefore, unlike *flex*MOF(CN)-I, *ex-flex*MOF(CN)-II was activated at room temperature under vacuum overnight. Through the sorption experiment, it was confirmed that tendency of carbon dioxide sorption was changed according to activation condition (figure 3.2.7). In the case of other flexible MOFs, such as *flex*MOF(CH_2), *flex*MOF(CH_3), and *flex*MOF(CN)-I, it was confirmed that the adsorption amount increased when activating at high temperature under vacuum. However, except for *flex*MOF(CN)-II, the adsorption amount decreased and the crystallinity was lost when activating at high temperature.

Although identical starting materials were used in the synthesis, CO_2 adsorption tendency of *flex*MOF(CN)-I and *flex*MOF(CN)-II was totally different from the solvent conditions of synthesis because the connectivity of the structure was differently synthesized according to the synthetic solvent (figure 3.2.2.). As shown in figure 3.1.2. and 3.2.2., the simplified structure of *flex*MOF(CN)-I and *flex*MOF(CN)-II can be compared, clearly confirming the difference in connectivity between ligand and metal. Besides, in the light of the analysis of the structure of *flex*MOF(CN)-I and *flex*MOF(CN)-II, the difference in degree of rotation of the macrocycle was observed. In the case of *flex*MOF(CN)-I, two hydrogen bonds are break down and two new hydrogen bonds are formed with rotating macrocycle, and then with cell shrinkage. On the other hand, in the case of flexMOF(CN)-II, after the activation, the rotation of the macrocycle still occurred, but it did not observe the phenomenon of forming a new hydrogen bond as the hydrogen bond was broken. I think that the hydrogen bond breaking and the newly formed phenomenon are important factors to cause the steep CO_2 adsorption. This is because the rotation of the macrocycle leads to spatial allowance for CO_2 adsorption. For this reason, *flex*MOF(CN)-I and *flex*MOF(CN)-II shown different sorption tendencies.

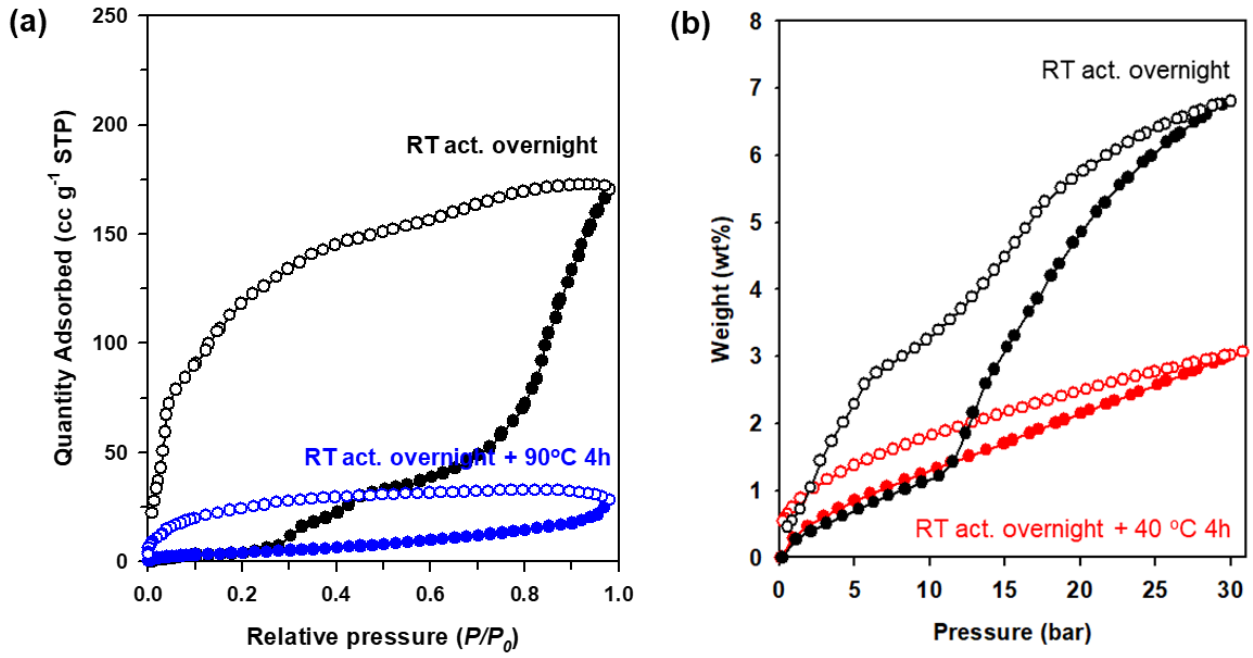

Figure 3.2.8. CO_2 sorption isotherm of *flex*MOF(CN)-II (a) CO_2 sorption isotherms of *flex*MOF(CN)-II at 195 K under low pressure (R.T under vacuum overnight, black; R.T under vacuum overnight + 90°C 4h, blue) (b) CO_2 sorption isotherms of *flex*MOF(CN)-II at 298 K under high pressure (R.T under vacuum overnight, black; R.T under vacuum overnight + 40°C for 4 h under vacuum, red)

III. 3. *flex*-MOF(CH_2)

The single crystal can be obtained by controlling MeCN:H_2O ratio through self-assembly method, which was analyzed through single crystal X-ray diffraction in Pohang Accelerator Laboratory. The diffraction data were collected at 100 K, and were measured in both mother liquor and dried states. Also, *as*-*flex*MOF(CH_2) was exchanged with distilled MeCN, followed by activation at 100 ºC for 4h, and then *d*-*flex*MOF(CH_2) can be obtained. As a result of analyzing the SCD data before and after drying, cell shrinkage could be quantified specifically and it was confirmed that the rotation of macrocycle occur while changing from *as*-*flex*MOF(CH_2) to *d*-*flex*MOF(CH_2). In the case of *flex*MOF(CH_2), during drying process, the new hydrogen bonds (pink) are formed with breaking the hydrogen bonds (green) (figure 3.3.1.). As shown below, in the case of *flex*MOF(CH_2), asymmetric unit is divided into two parts, Ni1A and Ni2B. In the case of Ni1A, there are four hydrogen bonds, and the interaction of hydrogen bonding do not change during drying process, but the rotation of macrocycle occurs. On the other hand, in the case of Ni2B, the hydrogen bonding of pale green color (figure 3.3.1.), was broken for drying process, and then new hydrogen bonding of pink color was formed between N and O.

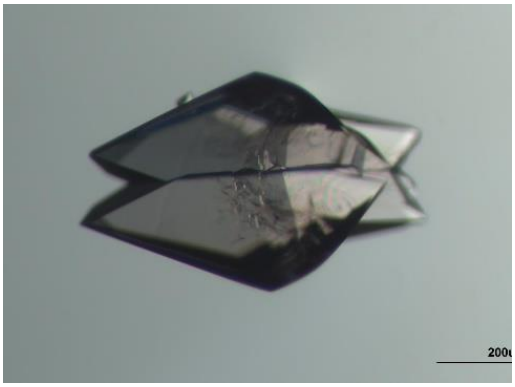

Figure 3.3.1. The microscope image of *flex*MOF(CH_2)

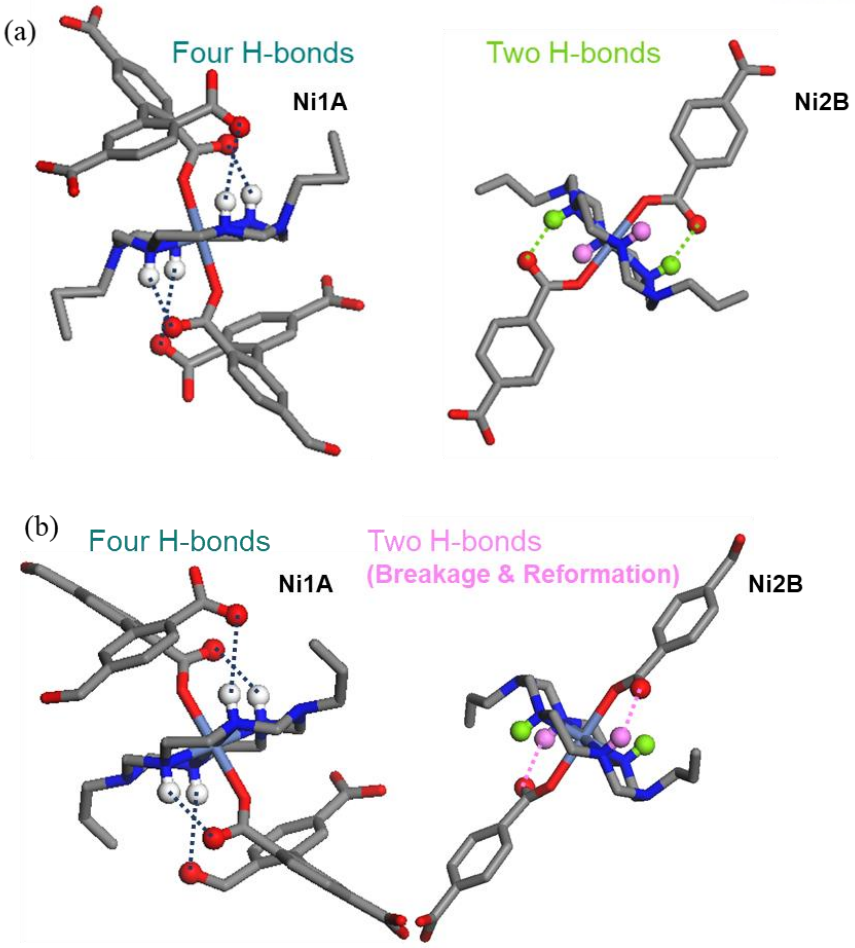

Figure 3.3.2. Comparison of hydrogen bonding for changing *as-flex*MOF(CH_2) to *d-flex*MOF(CH_2)

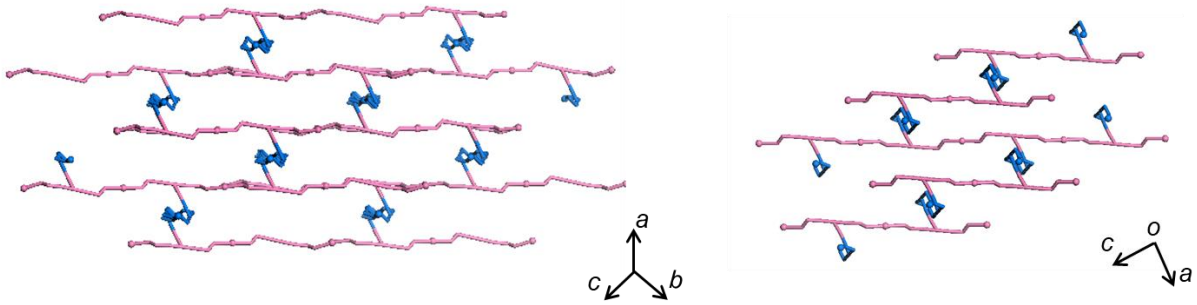

Figure 3.3.3. Simplified structure of *flex*MOF(CH_2), figure 3 in the same way as previous method (a) simplified structure of *as-flex*MOF(CH_2) from the perspective of a*bc* plane, (b) simplified structure of *d-flex*MOF(CH_2) from the perspective of *ca* plane.

Also, in figure 3.3.2., the simplified structure of *flex*MOF(CH_2) was drawn using MS modeling program. In the case of *flex*MOF(CH_2), it is classified as type II according to the above classification. Type II consist of *flex*MOF(CH_2), *flex*MOF(OH), and *flex*MOF(CN)-I, and all the materials have the same connectivity, but the angle between the metal and ligand is somewhat different. Through detailed analysis of SCD, I measured specific values for dihedral angle and cell shrinkage (figure 3.3.3.and 3.3.4). When changing from *as-flex*MOF(CH_2) to *d-flex*MOF(CH_2), the change of dihedral angle is clearly shown in table 3.3.1. There was a slight change overall in the rest except 2 and 5.

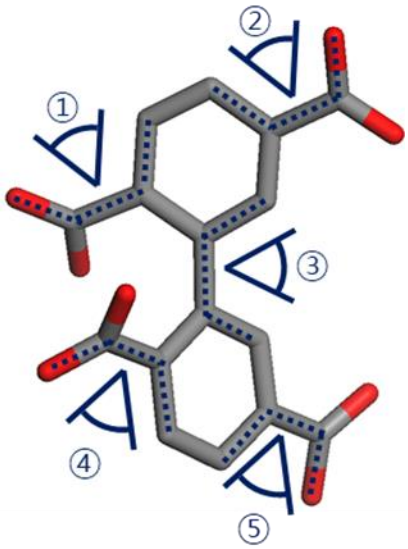

Figure 3.3.4. Dihedral angle of *flex*MOF(CH_2)

Table 3.3.1. dihedral angle table of *flex*MOF(CH_2)

angle	***as-flex*MOF(CH_2)**	***d-flex*MOF(CH_2)**
①	-134.842°	-136.825°
②	-170.251°	-169.314°
③	54.870°	57.681°
④	-126.962°	-130.447°
⑤	171.879°	170.617°

Also, specific length was measured by using MS modeling program to determine the rectangular dimension through SCD analysis, as shown in figure 3.3.4, the rectangular dimension of *flex*MOF(CH_2) decreased from 12.74 × 32.56 $Å^2$ to 9.85 × 32.79 $Å^2$ after activation, (for *as-flex*MOF(CH_2) and *d-flex*MOF(CH_2), respectively). This phenomena is that The rotation of macrocycle is caused to change

the dihedral angle of BPTC, and result in shrinkage of the cell for activation.

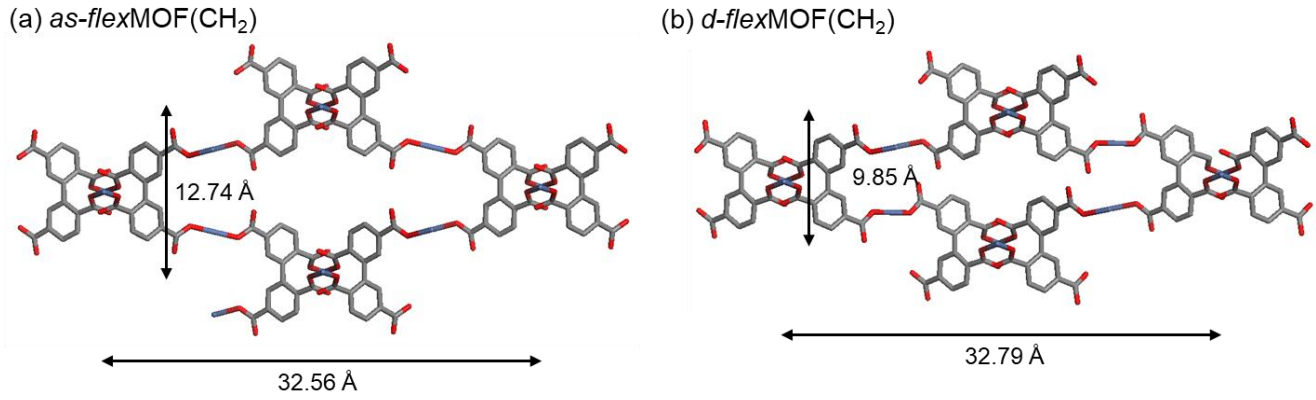

Figure 3.3.5. Change of cell size when activating *flex*MOF(CH_2)

Table 3.3.2. X-ray crystallographic data of *as-flex*MOF(CH_2)

Compound	*as-flex*MOF(CH_2)
Formula	C44 H66 N12 Ni2 O8
crystal system	*Monoclinic*
space group	$P2_1/n$
Fw	1008.50
a, Å	12.674(3)
b, Å	32.200(6)
c, Å	15.504(3)
α, deg	90
β, deg	104.30(3)
γ, deg	90
V, Å^3	6131(2)
Z	4
ρ_{calcd}, g cm^{-3}	1.093
temp , K	100
λ, Å	
μ, mm^{-1}	0.635
goodness-of-fit (F^2)	1.170
F(000)	2136
reflections collected	61977
independent reflections	19199 [R(int) = 0.0642]
completeness to θ_{max}, %	94.1
data/parameters/restraints	19199 / 599 / 14
θ range for data collection, deg	1.473 to 33.294°
diffraction limits (*h*, *k*, *l*)	-17<=h<=17, -46<=k<=46, -21<=l<=21
refinement method	Full-matrix least-squares on F^2
R_1, wR_2 [$I>2\sigma(I)$]	0.1124, 0.3393
R_1, wR_2 (all data)	0.1884, 0.3868
largest peak, hole, eÅ^{-3}	2.900, -1.615

$^aR = \Sigma||F_o| - |F_c||/\Sigma|F_o|$. $^bwR(F^2) = [\Sigma w(F_o^2 - F_c^2)^2/\Sigma w(F_o^2)^2]^{1/2}$ where $w = 1/[\sigma^2(F_o^2) + (0.2000P)^2]$, $P = (F_o^2 + 2F_c^2)/3$.

Table 3.3.3. X-ray crystallographic data of *d-flex*MOF(CH_2)

Compound	*d-flex*MOF(CH_2)
Formula	C44 H66 N12 Ni2 O8
crystal system	*Triclinic*
space group	*P-1*
Fw	1008.50
a, Å	9.829(3)
b, Å	14.867(3)
c, Å	16.595(4)
α, deg	90.112(7)
β, deg	78.434(10)
γ, deg	87.888(10)
V, Å^3	2374.0(10)
Z	2
ρ_{calcd}, g cm^{-3}	1.411
temp , K	100
λ, Å	
μ, mm^{-1}	0.820
goodness-of-fit (F^2)	1.045
F(000)	1068
reflections collected	23977
independent reflections	13223 [R(int) = 0.0934]
completeness to θ_{max}, %	92.2
data/parameters/restraints	13223 / 601 / 6
θ range for data collection, deg	1.820 to 33.225°
diffraction limits (*h*, *k*, *l*)	-13<=h<=13, -22<=k<=22, -25<=l<=25
refinement method	Full-matrix least-squares on F^2
R_1, wR_2 [$I>2\sigma(I)$]	0.1213, 0.3120
R_1, wR_2 (all data)	0.2601, 0.3788
largest peak, hole, eÅ^{-3}	0.797, -0.535

$^aR = \Sigma||F_o| - |F_c||/\Sigma|F_o|$. $^bwR(F^2) = [\Sigma w(F_o^2 - F_c^2)^2/\Sigma w(F_o^2)^2]^{1/2}$ where $w = 1/[\sigma^2(F_o^2) + (0.1648P)^2 + (1.1882)P]$, $P = (F_o^2 + 2F_c^2)/3$.

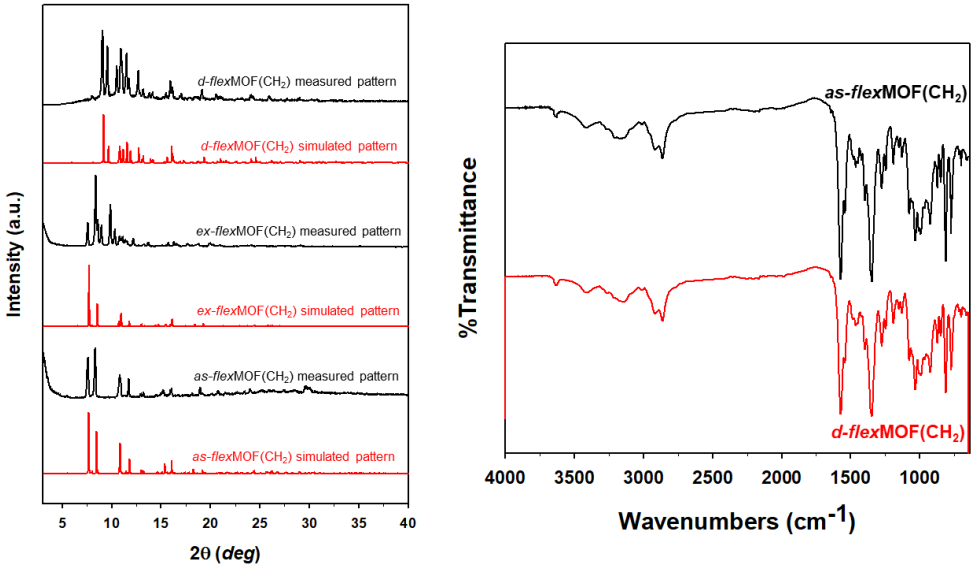

Figure 3.3.6. XRD graph and IR spectrum of *flex*MOF(CH_2) (a) Comparison of simulated pattern and measured pattern from *as-flex*MOF(CH_2) to *d-flex*MOF(CH_2) (simulated pattern, red; measured pattern, black) (b) IR spectrum of *flex*MOF(CH_2) (*d-flex*MOF(CH_2), red; *as-flex*MOF(CH_2), black)

In figure 3.3.5. XRD data and Infra-red spectroscopy is for *as-flex*MOF(CH_2) and *d-flex*MOF(CH_2), respectively. Both *as-flex*MOF(CH_2) and *d-flex*MOF(CH_2) is well matched with simulated pattern in XRD data. In the IR spectroscopic data, it was confirmed that the coordination bond between metal and ligand was intact by keeping the carboxylate peak at 1650 cm^{-1} after activation. TGA and EA were simultaneously measured in same vial sample, and through the calculation, the number of solvents in the pores could be determined as {[(NiL_{CH2})$_2$BPTC]·1MeCN·5H_2O} (figure 3.3.6.).

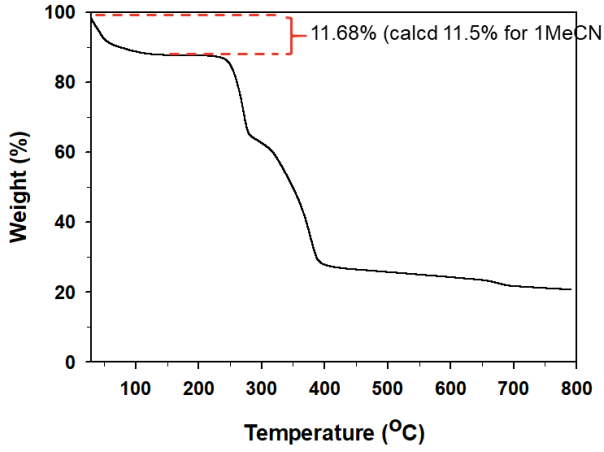

EA Results	1st	2nd	3rd	Calculated value
Carbon %	48.48	48.97	47.98	48.48
Hydrogen %	6.24	6.16	6.49	6.99
Nitrogen %	16.01	15.85	15.88	15.98
C/N ratio	3.53	3.60	3.52	3.54

Figure 3.3.7. (a) TGA trace of *as-flex*MOF(CH_2), (b) Result of Elemental Analysis

Gas sorption property

CO_2 sorption experiment were conducted in order to comprehend sorption property of flexMOF(CH_2), and sample preparation proceeded as follows. *as-flex*MOF(CH_2) was washed with MeCN:H_2O = 2:1 (v/v) to eliminate the unreacted precursor such as macrocycle, ligand, and TEA. And then exchange with distilled MeCN 2 times a day in total for 6 times. The exchanged sample, *ex-flex*MOF(CH_2), was introduced into the cell and activated at room temperature overnight under vacuum, followed by further 4 hours at 110 ºC under vacuum. In control experiment of activation condition, it was experimentally confirmed that increasing the temperature leads to loss of crystallinity, but increase in adsorption amount. Unlike *flex*MOF(CN)-II, *flex*MOF(CH_2) show higher adsorption amount when activated at high temperature. Through the sorption experiment under low / high pressure, it was confirmed that tendency of carbon dioxide sorption was changed according to activation condition (figure 3.3.7).

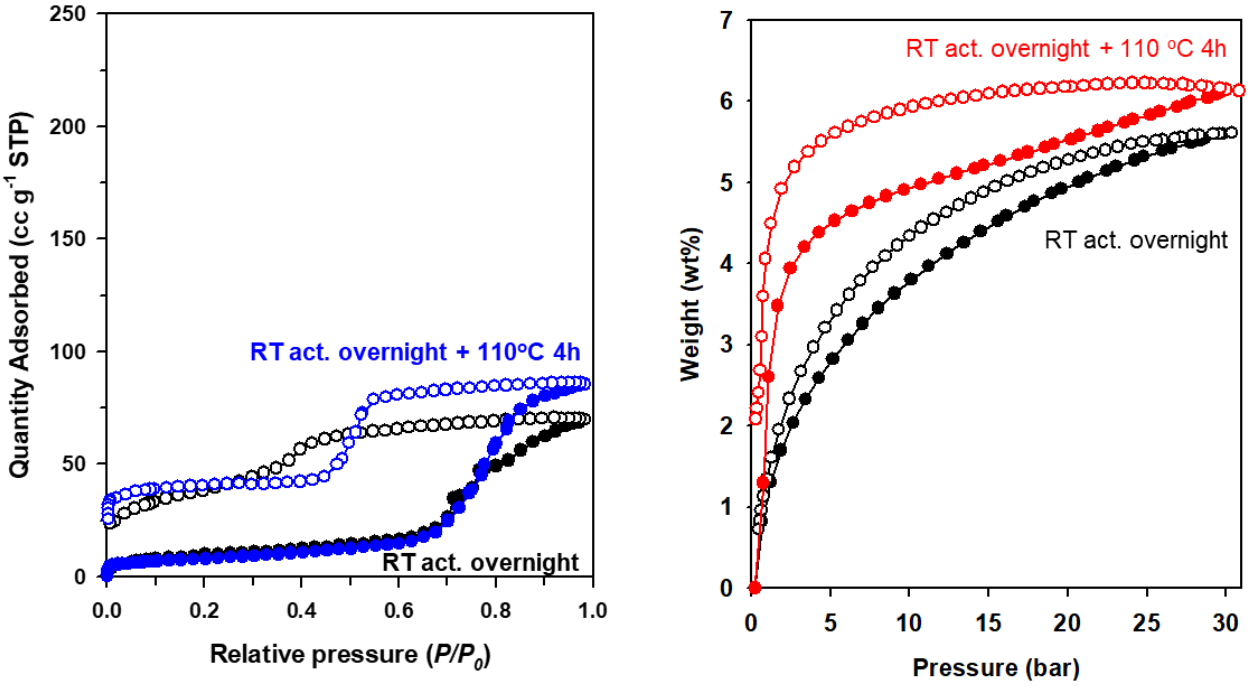

Figure 3.3.8. CO_2 sorption isotherm of *flex*MOF(CH_2) (a) CO_2 sorption isotherms of *flex*MOF(CH_2) at 195 K under low pressure (R.T under vacuum overnight, black; R.T under vacuum overnight + 110ºC 4h, blue) (b) CO_2 sorption isotherms of *flex*MOF(CH_2) at 298 K under high pressure (R.T under vacuum overnight, black; R.T under vacuum overnight + 110ºC for 4 h under vacuum, red)

III. 4. *flex*-MOF(OH)

*flex*MOF(OH) is synthesized as single crystal under DMF and H_2O mixture condition. *flex*MOF(OH) was needle-shaped crystals synthesized by shaking method (figure 3.4.1.), and stored at 10 °C for 3 days in order to grow the crystals larger and stronger. It was analyzed through single crystal X-ray diffraction in Pohang Accelerator Laboratory. The diffraction data were collected at 100 K, and were measured in both mother liquor and dried states. The sampling preparation method is as follows.

*as-flex*MOF(OH) is washed two times with DMF/H_2O mixture of identical ratio to remove the unreacted precursor. Then, the washed *as-flex*MOF(OH) is immersed in distilled THF 6 times for 3 days. After that process, *ex-flex*MOF(OH) is activated at room temperature under vacuum overnight, and activated additionally at 110 °C for 4 h under vacuum, and then *d-flex*MOF(OH) can be obtained. Using the synthesized materials, TGA, XRD, IR, EA, SCD, and sorption experiment were conducted for *as-flex*MOF(OH) and *d-flex*MOF(OH), respectively. SCD data result of *as-flex*MOF(OH) and *d-flex*MOF(OH) show that the tendency of hydrogen bonding was different from that of other *flex*MOF (figure 3.4.1.). In figure 3.4.1, (a) and (b) represent asymmetric unit of *as-flex*MOF(OH) and *d-flex*MOF(OH)

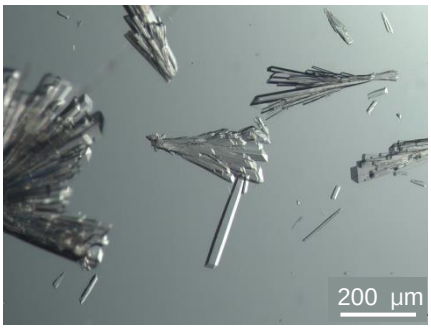

Figure 3.4.1. The microscope image of *flex*-MOF(OH)

In figure 3.4.2, the number of hydrogen bonds of *flex*MOF(OH) is compared before and after activation. In the case of *d-flex*MOF(OH), there are more hydrogen bonds in frameworks when compared with *as-flex*MOF(OH). Unlike other *flex*MOFs, it has more hydrogen bonds after activation, which makes it difficult for the shrunken cell to expand reversibly. More hydrogen bonds make the framework-framework interaction stronger, which hinders the rotation of the macrocycle.

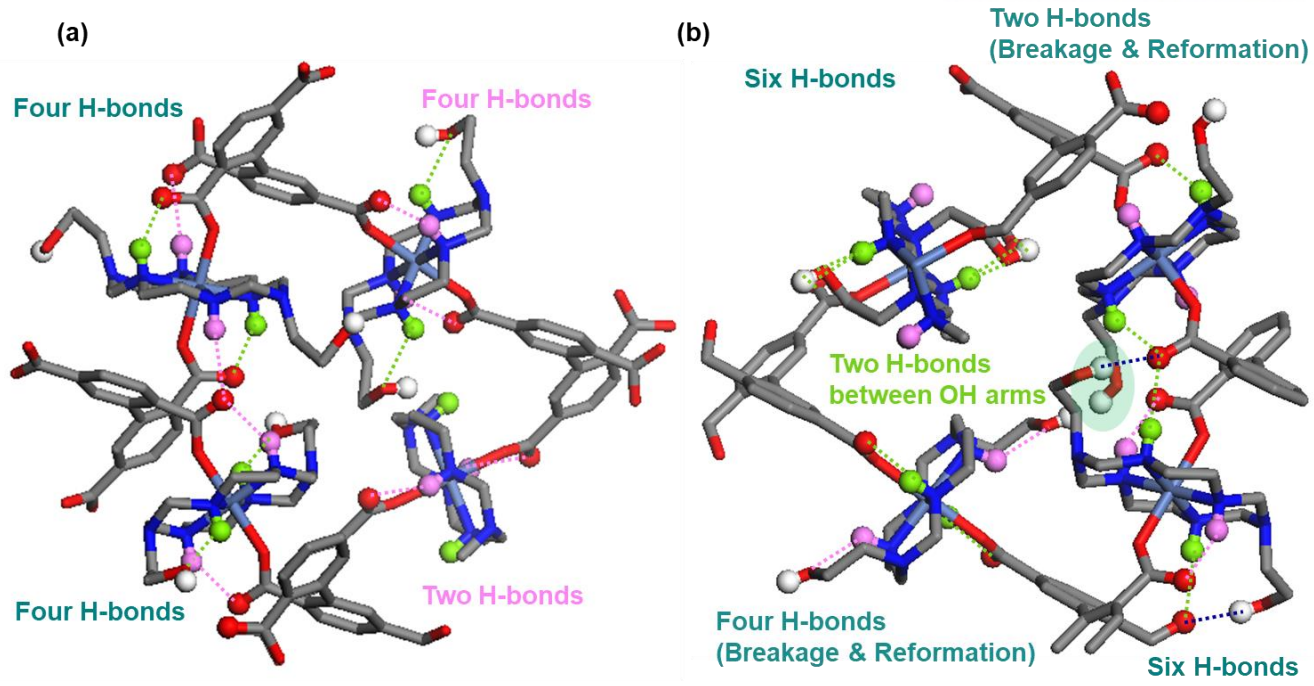

Figure 3.4.2. Comparison of hydrogen bonding for changing *as-flex*MOF(OH) to *d-flex*MOF(OH)

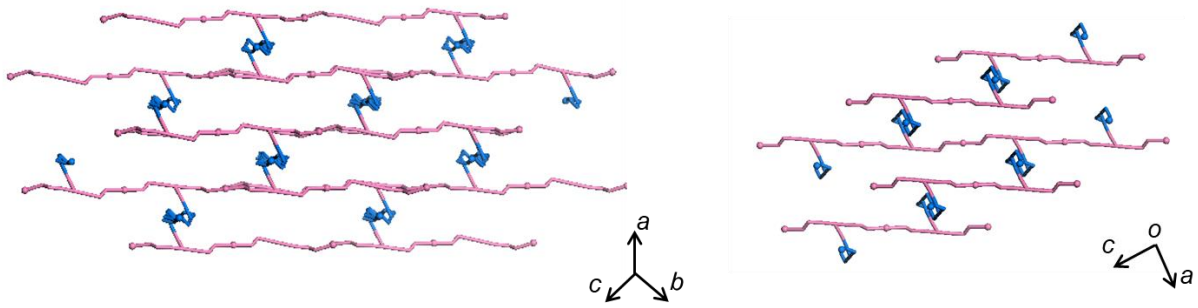

Figure 3.4.3. Simplified structure of *flex*MOF(OH), figure 3 in the same way as previous method (a) simplified structure of *as-flex*MOF(OH) from the perspective of a*bc* plane, (b) simplified structure of *d-flex*MOF(OH) from the perspective of *ca* plane.

As a result of analyzing the dihedral angle change, there are large change from 125.515° to 140.576° and from 9.605° to -162.023° in part 4, 5 respectively. It means that the cell shrinkage occurs significantly for activation and numerous hydrogen bonds occur between frameworks, which can make a interpretation of the phenomenon observed in CO_2 sorption experiments.

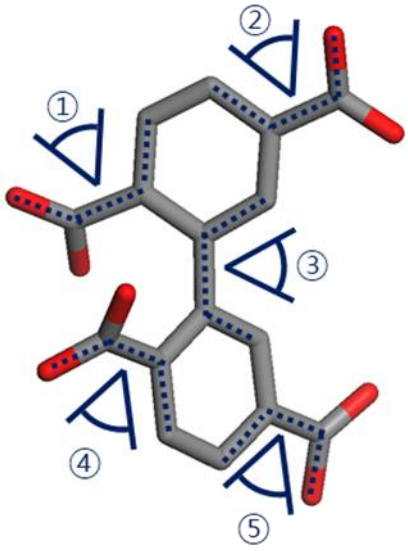

Figure 3.4.4. Dihedral angle of *flex*MOF(OH)

Table 3.4.1. dihedral angle table of *flex*MOF(OH)

angle	***as-flex*MOF(OH)**	***d-flex*MOF(OH)**
①	-138.304 º	-118.884 º
②	174.209 º	164.363 º
③	51.088 º	63.996 º
④	125.515 º	140.576 º
⑤	9.605 º	-162.023 º

Also, specific length was measured by using MS modeling program to determine the rectangular dimension through SCD analysis, as shown in figure 3.4.5, the rectangular dimension of *flex*MOF(OH) decreased from 14.94 × 30.68 Å^2 to 9.88 × 31.75 Å^2 after activation, (for *as-flex*MOF(OH) and *d-flex*MOF(OH), respectively). The phenomena is that The rotation of macrocycle is caused to change the dihedral angle of BPTC, and result in shrinkage of the cell for activation.

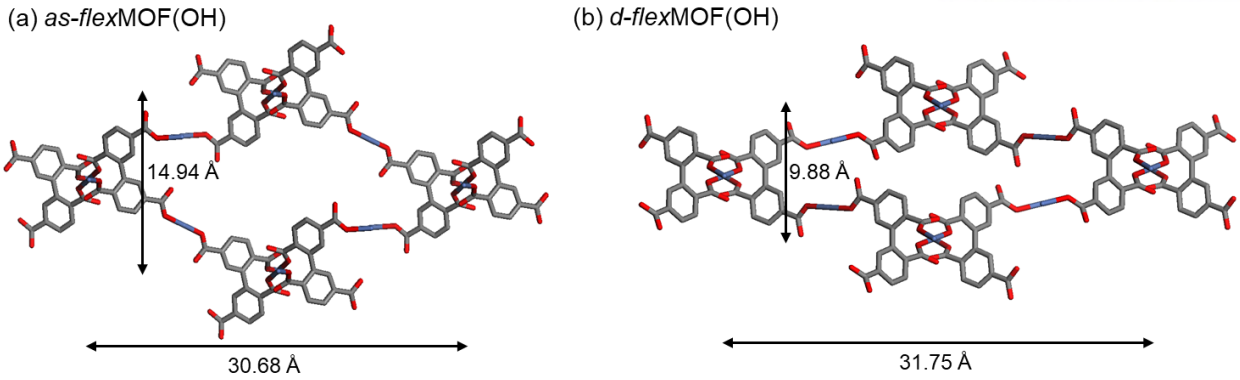

Figure 3.4.5. Change of cell size when activating *flex*MOF(OH)

Table 3.4.2. X-ray crystallographic data of *as-flex*MOF(OH)

Compound	*as-flex*MOF(OH)
Formula	C39 H64 N12 Ni2 O11
crystal system	*Triclinic*
space group	*P-1*
Fw	994.44
a, Å	14.939(4)
b, Å	15.608(4)
c, Å	16.860(4)
α, deg	82.135(10)
β, deg	65.407(7)
γ, deg	75.055(10)
V, Å^3	3451.7(15)
Z	2
ρ_{calcd}, g cm^{-3}	0.957
temp , K	100
λ, Å	0.700
μ, mm^{-1}	0.566
goodness-of-fit (F^2)	1.028
F(000)	1052
reflections collected	33940
independent reflections	19312 [R(int) = 0.0772]
completeness to θ_{max}, %	91.4
data/parameters/restraints	19312 / 587 / 16
θ range for data collection, deg	1.559 to 33.048°
diffraction limits (*h*, *k*, *l*)	-21<=h<=21, -20<=k<=20, -23<=l<=23
refinement method	Full-matrix least-squares on F^2
R_1, wR_2 [I>2σ(I)]	0.1161, 0.3516
R_1, wR_2 (all data)	0.2210, 0.3997
largest peak, hole, eÅ^{-3}	1.197, -1.150

[a] $R=\Sigma||F_o| - |F_c||/\Sigma|F_o|$. [b] $wR(F^2) = [\Sigma w(F_o^2 - F_c^2)^2/\Sigma w(F_o^2)^2]^{1/2}$ where $w = 1/[\sigma^2(F_o^2) + (0.1945P)^2]$, $P = (F_o^2 + 2F_c^2)/3$.

Table 3.4.3. X-ray crystallographic data of *d-flex*MOF(OH)

Compound	*d-flex*MOF(OH)
Formula	C40 H66 N12 Ni2 O12
crystal system	*Triclinic*
space group	*P-1*
Fw	1024.46
a, Å	9.819(3)
b, Å	15.316(3)
c, Å	16.301(3)
α, deg	90.994(10)
β, deg	103.450(7)
γ, deg	90.421(10)
V, Å^3	2383.7(10)
Z	2
ρ_{calcd}, g cm^{-3}	1.427
temp , K	100
λ, Å	0.700
μ, mm^{-1}	0.824
goodness-of-fit (F^2)	0.988
F(000)	1084
reflections collected	24060
independent reflections	13226 [R(int) = 0.0429]
completeness to θ_{max}, %	92.0
data/parameters/restraints	13226 / 605 / 1
θ range for data collection, deg	1.803 to 32.838°
diffraction limits (*h*, *k*, *l*)	-14<=h<=14, -21<=k<=21, -23<=l<=23
refinement method	Full-matrix least-squares on F^2
R_1, wR_2 [$I>2\sigma(I)$]	0.1003, 0.2839
R_1, wR_2 (all data)	0.1862, 0.3475
largest peak, hole, eÅ^{-3}	0.961, -0.764

[a] $R = \Sigma||F_o| - |F_c||/\Sigma|F_o|$. [b] $wR(F^2) = [\Sigma w(F_o^2 - F_c^2)^2/\Sigma w(F_o^2)^2]^{1/2}$ where $w = 1/[\sigma^2(F_o^2) + (0.2000P)^2 + (1.0852)P]$, $P = (F_o^2 + 2F_c^2)/3$.

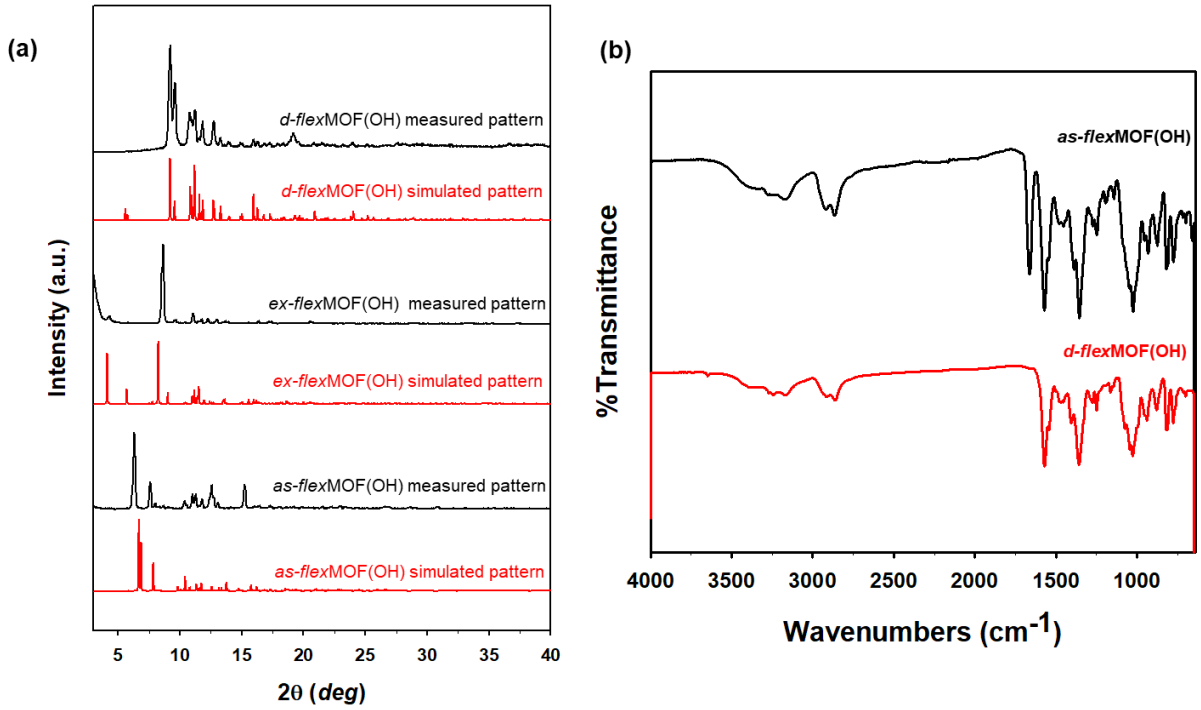

Figure 3.4.6. XRD graph and IR spectrum of *flex*MOF(OH) (a) Comparison of simulated pattern and measured pattern from *as-flex*MOF(OH) to *d-flex*MOF(OH) (simulated pattern, red; measured pattern, black) (b) IR spectrum of *flex*MOF(OH) (*d-flex*MOF(OH), red; *as-flex*MOF(CH_2), black)

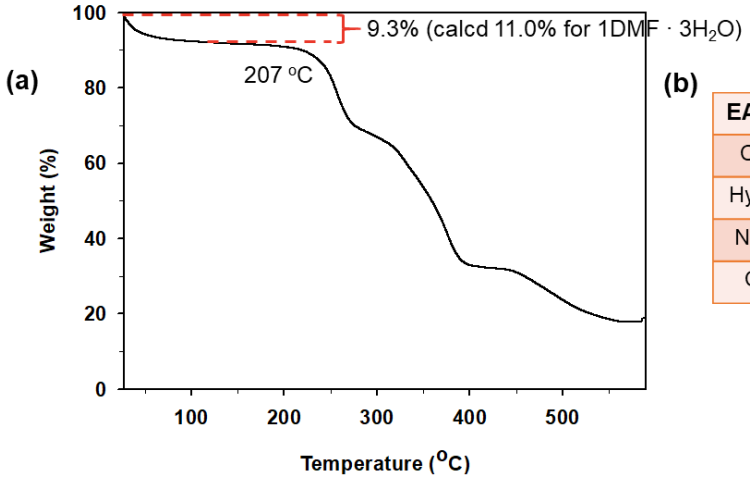

(b)

EA Results	1st	2nd	3rd	Calculated value
Carbon %	44.86	43.90	44.64	44.55
Hydrogen %	6.79	6.50	6.94	6.73
Nitrogen %	15.72	15.57	15.88	15.59
C/N ratio	3.33	3.29	3.28	3.33

Figure 3.4.7. (a) TGA trace of *as-flex*MOF(OH), (b) Result of Elemental Analysis

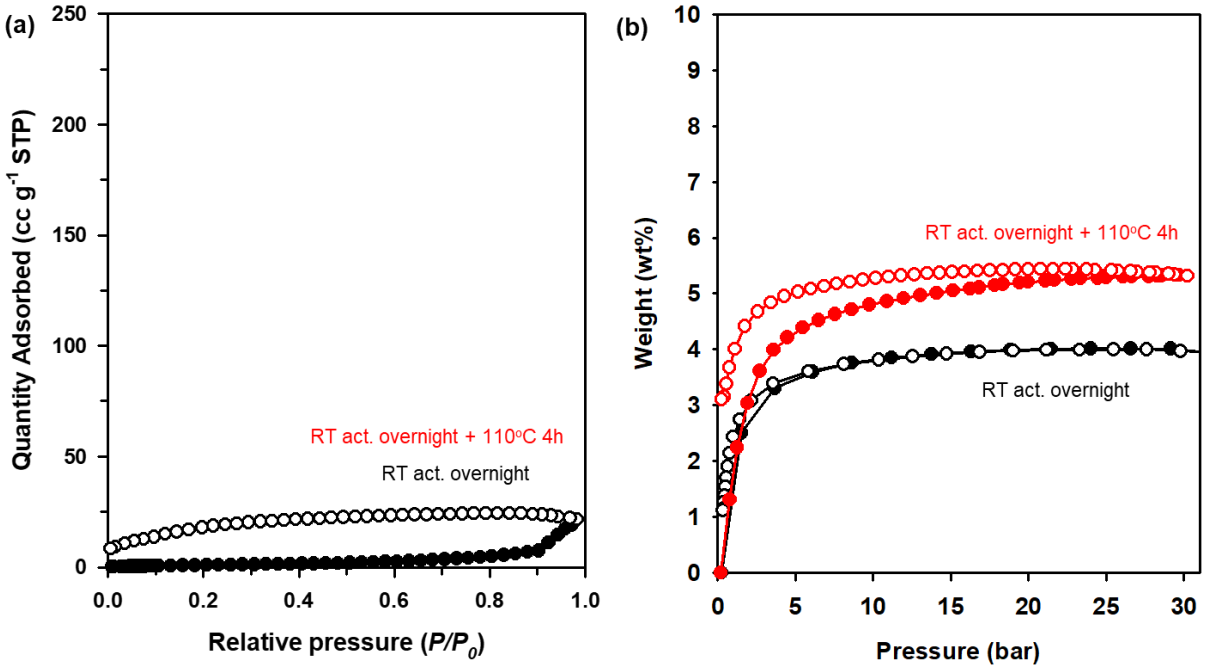

Figure 3.4.8. CO_2 sorption isotherm of *flex*MOF(OH) (a) CO_2 sorption isotherms of *flex*MOF(OH) at 195 K under low pressure (R.T under vacuum overnight, black; R.T under vacuum overnight + 110°C 4h, blue) (b) CO_2 sorption isotherms of *flex*MOF(OH) at 298 K under high pressure (R.T under vacuum overnight, black; R.T under vacuum overnight + 110°C for 4 h under vacuum, red)

IV. Conclusion

In summary, we systematically demonstrated novel approach that can fine-tune the gate-opening pressure by adjusting functional group of macrocycle arm. Most of all, five kinds of flexible MOFs, denoted as *flex*MOF(CH_3), *flex*MOF(CN)-I, *flex*MOF(CN)-II, *flex*MOF(CH_2), and *flex*MOF(OH), are successfully synthesized in the form of single crystal through the self-assembly method which is able to easily adjust solubility. Also, the structural changes were investigated through SCD analysis during the transition from *as-flex*MOF to *d-flex*MOF, and anticipated what happens in the intermediate stage. In macrocycle-based MOFs, the only report is that several functional groups of the macrocycle is introduced to tune the gate-opening pressure of MOFs. In a previously reported paper[ref], it was confirmed that the interaction between the functional group corresponding to the arm of the macrocycle and CO_2 exists, and we realized that the interaction between functional group of macrocycle arm and CO_2 plays important role in causing the gate-opening phenomenon. So, by using metal cluster which can rotate and introduce various functional groups-allyl, nitrile, methyl, and hydroxyl, we have successfully implemented both gate-opening and breathing phenomena in one system.

Herein, we focused on research to understand the difference of dynamic behavior according to functional groups, synthetic condition, connectivity of the structure, and activation condition. To understand the phenomenon in more detail, gas sorption isotherms were measured under low pressure / high pressure at various temperature condition and activation methods. Through sorption experiments under various condition, the sorption tendency about each factor could be comprehended. Most of all, among the several kinds of gases, only the case of CO_2 was able to cause the gate opening phenomenon by the interaction with the frameworks. For the other gases – N_2, H_2, and CH_4, the host-host interaction was too stronger than the guest-host interaction to trigger the gate-opening behavior, so neither gate-opening nor breathing phenomenon has been observed because guest-host interaction is insufficient to rotate the macrocycle. In addition, the degree of contraction of the frameworks affect dynamic behavior, which is divided into several factors – solvent-framework interaction, connectivity of the structure, steric effect, and the interaction between functional group and guest.

In spite of the detailed study performed about flexible MOFs, however, there are still many interesting questions and it will be covered in the future. To further investigate the effect of functional groups on flexibility, the study of the rotational energies and interaction sites with regard to functional groups is underway through computational simulations. Overall, the findings will provide useful information for fine-tuning flexible MOFs, and it will present a new perspective different from the previous one.

II. 5. Reference

(1) Kitagawa, S.; Uemura, K. Dynamic Porous Properties of Coordination Polymer Inspired by Hydrogen bonds. *Chem. Soc. Rev.*, **2005**, *34*, 109–119.

(2) Yaghi, O. M.; O'Keeffee, M.; Ockwig, N.W.; Chae, H. K.; Eddaoudi, M & Kim, J. Reticular Synthesis and The design of New Materials. *Nature*. **423**. 705-714 (2003).

(3) Kitagawa, S.; Horike, S.; Shimomura, S. Soft porous crystals. *Nature chemistry*. **2009**, 695-704.

(4) Fischer, R. A.; Schneemann, A.; Bon, V.; Schwedler, I.; Senkovska, I.; Kaskel, S. Flexible Metal-Organic Frameworks. *Chem. Soc. Rev.* **2014**, *43*, 6062–6096.

(5) Fischer, R. A.; Henke, S.; Schneemann, A.; Wutscherm A. Directing the Breathing Behavior of Pillared-Layered Metal-Organic Frameworks via a Systematic Library of Functionalized Linkers Bearing Flexible Substituents. *J. Am. Chem. Soc.* **2012**, *134*, 9464–9474.

(6) Fischer, R. A.; Henke, S.; Schneemann, A.; Vervoorts, P.; Hante, I.; Tu, M.; Wannapaiboon, S.; Sternemann, C.; Paulus, M. Different Breathing Mechanisms in Flexible Pillared-Layered Metal-Organic Frameworks: Impact of the Metal center. *Chem. Mater.* **2018**, *30*, 1667–1676.

(7) Moon, H. R.; Moon, D.; Kwak, S. K.; Hyun, S.; Lee, J. H.; Jung, G. Y.; Kim, Y. K.; Kim, T. K.; Jeoung, S. Exploration of Gate-Opening and Breathing Phenomena in a Tailored Flexible Metal-Organic Framework. *Inorg. Chem.* **2016**, *55*, 1920-1925.

(8) Barbour, L. J.; Nikolayenko, V. I.; Herbert S .A. Non-Precious Alloy Encapsulated in Nitrogen-Doped Graphene Layers Derived from MOFs as an Active and Durable Hydrogen Evolution Reaction Catalyst. *Energy Environ. Sci.* **2015**, *8*, 3563–3571.

(9) Lu, X.-F.; Gu, L.-F.; Wang, J.-W.; Wu, J.-X.; Liao, P.-Q.; Li, G.-R. Bimetal-Organic Framework Derived $CoFe_2O_4$/C Porous Hybrid Nanorod Arrays as High-Performance Electrocatalysts for Oxygen Evolution Reaction. *Adv. Mater.* **2016**, *1604437*.

(10) Jeffrey R. L.; Masciocchi, N.; Jarad A. M.; Julia, O.; Mercedes, K.; Matthew, R.; Julien, R.; Jonathan, E. B.; Miguel, I. G.; Antonio, C.; Craig M, B.; Philip L. L. Methane storage in flexible metal-organic frameworks with intrinsic thermal management. *Nature latter*, **2015**, *527*, 357–361.

(11) Lee, B.; Elliot, J.; Craig A, M.; Ashleigh J. F.; Stephen, P. T. Solvent-switchable continuous-

breathing behaviour in a diamondoid metal-organic framework and its influence on CO_2 versus CH_4 selectivity. *Nature. Chemistry.* **2018**, *9*, 882–889.

(12) Jung, S. K; Kang, S. G.; Suh, M. P. Template Synthesis and Properties of Square Planar Nickel(II) and Copper(II) Complexes of 14-Membered Hexaaza Macrocyclic Ligands with Various Alkyl Pendant Arms at the Uncoordinated Nitrogens. *Kor. Chem. Soc.* **1989**, 1*0*, 362–366.

(13) Holy, P.; Sehanl, P.; Tichy, M.; Zavada, J.; Cisarova, I..Self-assembly of chiral hydrogen-bonded grid layers from terephthalic Siamese twins. *Tetrahedron: Asymmetry.* **2003**. *14*. 245-253.

(14) J. Barbour, L.; Prem, L. Distinctive Three-Step Hysteretic Sorption of Ethane with In-situ Crystallographic Visualization of the Pore Forms in a Soft Porous Crystal. *J. Am. Chem. Soc.* **2018**, *140*, 2145–2150.

(15) Kitagawa, S.; Matsuda, R.; Zheng, Y.; Sato, H.; Wu, P.; Jeon, H. J. Flexible interlocked porous frameworks allow quantitative photoisomerization in a crystalline solid. *Nature. Comm.* **2017**, *8*, 100.

(16) Zang, S.; Dong, X.; Huang, H.; Wang, J.; Li, H. A Flexible Fluorescent SCC-MOF for Switchable Molecule Identification and Temperature Display. *Chem. Mater.* **2018**, *30*, 2160–2167.

(17) Kitagawa, S.; Takata, M.; Kobayashi, T.; Tanaka, D.; Nakagawa, K.; Higuchi, M.; Horike, S.; Kubota, Y. Kinetic Gate-Opening Process in a Flexible Porous Coordination Polymer. *Angew. Chem. Int. Ed.* **2008**, *47*, 3914–3918.

(18) Bu, X.; Hu, T.; Chang, Z.; Yang, D.; Xu, J. Flexible Metal-Organic Frameworks : Recent Advances and Potential Applications. *Adv. Mater.* **2015**, *27*, 5432–5441.

(19) Kim, K.; Dybtsev, D.; Chun, H. Rigid and Flexible : A Highly Porous Metal-Organic Framework with Unusual Guest-Dependent Dynamic Behavior. *Angew. Chem. Int. Ed.* **2004**, *43*, 5033–5036.

(20) Zaworotko, M.; Kitagawa, S.; Space, B.; Hosono, N.; Forrest, K.A.; Chen, K. J.; Yang, Q.Y.; Sen, S.; Madden, D.; Kumar, A.; Pham, T. Efficient CO_2 Removal for Ultra-Pure CO production by Two Hybrid Ultramicroporous Materials. *Angew. Chem.* **2018**, *130*, 1-6.

(21) Chen, B.; Li, L.; Lin, R.; Krishna, R.; Wang, X.; Li, B.; Wu, H.; Li, J.; Zhou, W. Flexible-

Robust Metal-Organic Framework for Efficient Removal of Propyne form Propylene. *J. Am. Chem. Soc.* **2017**, *139*, 7733–7736.

(22) Paesani, F.; Gianneschi, N. C.; Parent, L. R.; Pham, C. H.; Patterson, J. P.; Denny, M. S.; Cohen, S. M. Pore Breathing of Metal-Organic Frameworks by Environmental Transmission Electron Microscopy. *J. Am. Chem. Soc.* **2017**, *139* (40), 13973–13976.

(23) Kitagawa, S.; Bonneau, C.; Seo, J.; Matsuda, R.; Sakamoto, H. A Pillared-Layer Coordination Polymer with a Rotatable Pillar Acting as a Molecular Gate for Guest Molecules. *J. Am. Chem. Soc*. **2009**, *131*, 12792–12800.

(24) Kitagawa, S.; Uemura, K. Dynamic porous properties of coordination polymer inspired by hydrogen bonds. *Chem. Soc. Rev.* **2005**, *34*, 109–119.

(25) Barbour, L. J.; Nikolayenko, V. I.; Herbert, S. A. Reversible structural switching of a metal-organic framework by photoirradiation. *Chem. Commun.* **2017**, *53*, 11142–11145.

(26) Xia, W.; Mahmood, A.; Zou, R.; Xu, Q. Metal-Organic Frameworks and Their Derived Nanostructures for Electrochemical Energy Storage and Conversion. *Energy Environ. Sci.* **2015**, *8* (7), 1837–1866.

(27) H. Furukawa, K. E. Cordova, M. O'Keeffe and O. M. Yaghi. The Chemistry and Applications of Metal-Organic Frameworks. *Science*, **2013**, *341*, 974.

(28) Millange, F.; Guillou, N.; Walton, R. I.; Greneche, J.-M.; Margiolaki, I.; Ferey, g. Very Large Breathing Effect in the First Nanoporpous Chromium(III)-Based Solid : MIL-53 or $Cr^{III}(OH)(O_2C\text{-}C_6H_4\text{-}CO_2)(HO_2C\text{-}C_6H_4\text{-}CO_2H)_x\ H_2O_y$. *J. Am. Chem. Soc.* **2002**, *124 (45)*, 13519-13526.

(29) Telfer, S. G.; Minnaar, J. L.; Deshpande, R. K. Thermolabile Groups in Metal-Organic Frameworks: Suppression of Network Interpenetration, Post-Synthetic Cavity Expansion, and Protection of Reactive Functional Groups. *Angew. Chem. Int. Ed.* **2010**, *49*, 4598-4602.

(30) Choe, W.; Hu, C.; Burnett, B. J.; Barron, P. M. Stepwise Synthesis of Metal-Organic Frameworks : Replacement of Structural Organic Linkers. *J. Am. Chem. Soc.* **2011**, *133* (26), 9984–9987.

(31) Yang, C.; Wang, X.; Omary, M. Crystallographic Observation of Dynamic Gas Adsorption Sites and Thermal Expansion in a Breathable Fluorous Metal-Organic Framework. *Angew. Chem. Int. Ed.* **2009**, *48*, 2500-2505.

(32) El-Sawy, A. M.; Mosa, I. M.; Su, D.; Guild, C. J.; Khalid, S.; Joesten, R.; Rusling, J. F.; Suib, S. L. Controlling the Active Sites of Sulfur-Doped Carbon Nanotube-Graphene Nanolobes for Highly Efficient Oxygen Evolution and Reduction Catalysis. *Adv. Energy Mater.* **2016**, *6* (5), 1–12.

(33) Liu, X.; Zhang, J.; Guo, S.; Pinna, N. Graphene/N-Doped Carbon Sandwiched Nanosheets with Ultrahigh Nitrogen Doping for Boosting Lithium-Ion Batteries. *J. Mater. Chem. A* **2016**, *4* (4), 1423–1431.

(34) Böttger-Hiller, F.; Mehner, A.; Anders, S.; Kroll, L.; Cox, G.; Simon, F.; Spange, S. Sulphur-Doped Porous Carbon from a Thiophene-Based Twin Monomer. *Chem. Commun. (Camb).* **2012**, *48* (85), 10568–10570.

(35) Xu, Q.; Pu, P.; Zhao, J.; Dong, C.; Gao, C.; Chen, Y.; Chen, J.; Liu, Y.; Zhou, H. Preparation of Highly Photoluminescent Sulfur-Doped Carbon Dots for Fe(iii) Detection. *J. Mater. Chem. A* **2015**, *3* (2), 542–546.

(36) Mueller, A.; Schwab, M. G.; Encinas, N.; Vollmer, D.; Sachdev, H.; M??llen, K. Generation of Nitrile Groups on Graphites in a Nitrogen RF-Plasma Discharge. *Carbon N. Y.* **2015**, *84* (1), 426–433.

(37) Han, P.; Yue, Y.; L; Dong, S.; Cui, E. Graphene Oxide Nanosheets/multi-Walled Carbon Nanotubes Hybrid as an Excellent Electrocatalytic Material towards VO2+/VO2+ Redox Couples for Vanadium Redox Flow Batteries. *Energy Environ. Sci.* **2011**, *4* (11), 4710.

(38) Xu, W.; Zhang, H.; Li, G.; Wu, Z. Nickel-Cobalt Bimetallic Anode Catalysts for Direct Urea Fuel Cell. *Sci. Rep.* **2014**, *4*, 5863.

(39) Mi, L.; Wei, W.; Huang, S.; Cui, S.; Zhang, W.; Hou, H.; Chen, W. A Nest-like Ni@Ni 1.4 Co 1.6 S 2 Electrode for Flexible High-Performance Rolling Supercapacitor Device Design. *J. Mater. Chem. A* **2015**, *3* (42), 20973–20982.

(40) Feng, L.-L.; Fan, M.; Wu, Y.; Liu, Y.; Li, G.-D.; Chen, H.; Chen, W.; Wang, D.; Zou, X. Metallic Co 9 S 8 Nanosheets Grown on Carbon Cloth as Efficient Binder-Free Electrocatalysts for Hydrogen Evolution Reaction under Neutral Media. *J. Name* **2015**, *0*, 1–3.

(41) Pan, Y.; Chen, Y.; Li, X.; Liu, Y.; Liu, C. Nanostructured Nickel Sulfides: Phase Evolution, Characterization and Electrocatalytic Properties for the Hydrogen Evolution Reaction. *RSC Adv.* **2015**, *5*, 104740–104749.

(42) Andreu, N.; Flahaut, D.; Dedryvère, R.; Minvielle, M.; Martinez, H.; Gonbeau, D. XPS Investigation of Surface Reactivity of Electrode Materials: Effect of the Transition Metal. *ACS Appl. Mater. Interfaces* **2015**, *7* (12), 6629–6636.

(43) Georgakilas, V.; Otyepka, M.; Bourlinos, A. B.; Chandra, V.; Kim, N.; Kemp, K. C.; Hobza, P.; Zboril, R.; Kim, K. S. Functionalization of Graphene: Covalent and Non-Covalent Approaches, Derivatives and Applications. *Chem. Rev.* **2012**, *112* (11), 6156–6214.

(44) Feng, L. L.; Li, G. D.; Liu, Y.; Wu, Y.; Chen, H.; Wang, Y.; Zou, Y. C.; Wang, D.; Zou, X. Carbon-Armored Co9S8 Nanoparticles as All-pH Efficient and Durable H2-Evolving Electrocatalysts. *ACS Appl. Mater. Interfaces* **2015**, *7* (1), 980–988.

Appendix

Table S1. The bond lengths [Å] and angles[°] around nickel metal of **as-*flex*MOF(CN)-I**

Ni(1)-N(1)$^{\#1}$	2.052(4)	Ni(3)-N(6)	2.027(4)
Ni(1)-N(1)	2.052(4)	Ni(3)-N(6)$^{\#2}$	2.027(4)
Ni(1)-N(2)$^{\#1}$	2.055(4)	Ni(3)-N(5)	2.065(4)
Ni(1)-N(2)	2.055(4)	Ni(3)-N(5)$^{\#2}$	2.065(4)
Ni(1)-O(2)$^{\#1}$	2.088(3)	Ni(3)-O(4)$^{\#2}$	2.096(3)
Ni(1)-O(2)	2.088(3)	Ni(3)-O(4)	2.096(3)
N(1)$^{\#1}$-Ni(1)-N(1)	180.0	N(6)-Ni(3)-N(6)$^{\#2}$	180.0
N(1)$^{\#1}$-Ni(1)-N(2)$^{\#1}$	94.43(17)	N(6)-Ni(3)-N(5)	94.23(18)
N(1)-Ni(1)-N(2)$^{\#1}$	85.57(17)	N(6)$^{\#2}$-Ni(3)-N(5)	85.77(18)
N(1)$^{\#1}$-Ni(1)-N(2)	85.57(17)	N(6)-Ni(3)-N(5)$^{\#2}$	85.77(18)
N(1)-Ni(1)-N(2)	94.43(17)	N(6)$^{\#2}$-Ni(3)-N(5)$^{\#2}$	94.23(18)
N(2)$^{\#1}$-Ni(1)-N(2)	180.0	N(5)-Ni(3)-N(5)$^{\#2}$	180.0(3)
N(1)$^{\#1}$-Ni(1)-O(2)$^{\#1}$	93.34(13)	N(6)-Ni(3)-O(4)$^{\#2}$	88.97(14)
N(1)-Ni(1)-O(2)$^{\#1}$	86.66(13)	N(6)$^{\#2}$-Ni(3)-O(4)$^{\#2}$	91.02(14)
N(2)$^{\#1}$-Ni(1)-O(2)$^{\#1}$	87.52(13)	N(5)-Ni(3)-O(4)$^{\#2}$	87.99(14)
N(2)-Ni(1)-O(2)$^{\#1}$	92.48(13)	N(5)$^{\#2}$-Ni(3)-O(4)$^{\#2}$	92.01(14)
N(1)$^{\#1}$-Ni(1)-O(2)	86.66(13)	N(6)-Ni(3)-O(4)	91.03(14)
N(1)-Ni(1)-O(2)	93.34(13)	N(6)$^{\#2}$-Ni(3)-O(4)	88.98(14)
N(2)$^{\#1}$-Ni(1)-O(2)	92.48(13)	N(5)-Ni(3)-O(4)	92.01(14)
N(2)-Ni(1)-O(2)	87.52(13)	N(5)$^{\#2}$-Ni(3)-O(4)	87.99(14)
O(2)$^{\#1}$-Ni(1)-O(2)	180.0	O(4)$^{\#2}$-Ni(3)-O(4)	180.0

Symmetry transformations used to generate equivalent atoms:

#1 : -x+1,-y,-z+1 #2 : -x+1/2,-y+1/2,-z #3 : -x+1,y,-z+1/2

Table S2. The bond lengths [Å] and angles[°] around nickel metal of ***d-flex*MOF(CN)-I**

Ni(1)-N(2)$^{\#1}$	2.043(5)	Ni(2)-N(6)$^{\#2}$	2.056(6)
Ni(1)-N(2)	2.043(5)	Ni(2)-N(6)	2.056(6)
Ni(1)-N(1)$^{\#1}$	2.045(5)	Ni(2)-N(5)$^{\#2}$	2.073(7)
Ni(1)-N(1)	2.045(5)	Ni(2)-N(5)	2.073(7)
Ni(1)-O(2)$^{\#1}$	2.179(4)	Ni(2)-O(4)$^{\#2}$	2.130(4)
Ni(1)-O(2)	2.179(4)	Ni(2)-O(4)	2.130(4)
Ni(3)-N(10)	2.042(5)	Ni(4)-N(13)$^{\#4}$	2.019(5)
Ni(3)-N(10)$^{\#3}$	2.042(5)	Ni(4)-N(13)	2.019(5)
Ni(3)-N(9)$^{\#3}$	2.053(5)	Ni(4)-N(14)$^{\#4}$	2.058(6)
Ni(3)-N(9)	2.053(5)	Ni(4)-N(14)	2.058(6)
Ni(3)-O(6)	2.153(4)	Ni(4)-O(8)	2.199(4)
Ni(3)-O(6)$^{\#3}$	2.153(4)	Ni(4)-O(8)$^{\#4}$	2.199(4)
N(2)$^{\#1}$-Ni(1)-N(2)	180.0	N(6)$^{\#2}$-Ni(2)-N(6)	180.0(4)
N(2)$^{\#1}$-Ni(1)-N(1)$^{\#1}$	91.91(19)	N(6)$^{\#2}$-Ni(2)-N(5)$^{\#2}$	86.2(3)
N(2)-Ni(1)-N(1)$^{\#1}$	88.09(19)	N(6)-Ni(2)-N(5)$^{\#2}$	93.8(3)
N(2)$^{\#1}$-Ni(1)-N(1)	88.09(19)	N(6)$^{\#2}$-Ni(2)-N(5)	93.8(3)
N(2)-Ni(1)-N(1)	91.91(19)	N(6)-Ni(2)-N(5)	86.2(3)
N(1)$^{\#1}$-Ni(1)-N(1)	180.0	N(5)$^{\#2}$-Ni(2)-N(5)	180.0
N(2)$^{\#1}$-Ni(1)-O(2)$^{\#1}$	90.05(17)	N(6)$^{\#2}$-Ni(2)-O(4)$^{\#2}$	92.4(2)
N(2)-Ni(1)-O(2)$^{\#1}$	89.95(17)	N(6)-Ni(2)-O(4)$^{\#2}$	87.6(2)
N(1)$^{\#1}$-Ni(1)-O(2)$^{\#1}$	88.30(17)	N(5)$^{\#2}$-Ni(2)-O(4)$^{\#2}$	93.7(2)
N(1)-Ni(1)-O(2)$^{\#1}$	91.71(17)	N(5)-Ni(2)-O(4)$^{\#2}$	86.3(2)
N(2)$^{\#1}$-Ni(1)-O(2)	89.95(17)	N(6)$^{\#2}$-Ni(2)-O(4)	87.6(2)
N(2)-Ni(1)-O(2)	90.05(17)	N(6)-Ni(2)-O(4)	92.4(2)
N(1)$^{\#1}$-Ni(1)-O(2)	91.70(17)	N(5)$^{\#2}$-Ni(2)-O(4)	86.3(2)
N(1)-Ni(1)-O(2)	88.30(17)	N(5)-Ni(2)-O(4)	93.7(2)
O(2)$^{\#1}$-Ni(1)-O(2)	180.0	O(4)$^{\#2}$-Ni(2)-O(4)	180.0(3)
N(10)-Ni(3)-N(10)$^{\#3}$	180.0	N(13)$^{\#4}$-Ni(4)-N(13)	180.0
N(10)-Ni(3)-N(9)$^{\#3}$	85.8(2)	N(13)$^{\#4}$-Ni(4)-N(14)$^{\#4}$	95.1(2)
N(10)$^{\#3}$-Ni(3)-N(9)$^{\#3}$	94.2(2)	N(13)-Ni(4)-N(14)$^{\#4}$	84.9(2)
N(10)-Ni(3)-N(9)	94.2(2)	N(13)$^{\#4}$-Ni(4)-N(14)	84.9(2)
N(10)$^{\#3}$-Ni(3)-N(9)	85.8(2)	N(13)-Ni(4)-N(14)	95.1(2)
N(9)$^{\#3}$-Ni(3)-N(9)	180.0(3)	N(14)$^{\#4}$-Ni(4)-N(14)	180.0

N(10)-Ni(3)-O(6)	91.3(2)	N(13)$^{\#4}$-Ni(4)-O(8)	93.26(19)
N(10)$^{\#3}$-Ni(3)-O(6)	88.7(2)	N(13)-Ni(4)-O(8)	86.75(19)
N(9)$^{\#3}$-Ni(3)-O(6)	91.4(2)	N(14)$^{\#4}$-Ni(4)-O(8)	86.7(2)
N(9)-Ni(3)-O(6)	88.6(2)	N(14)-Ni(4)-O(8)	93.3(2)
N(10)-Ni(3)-O(6)$^{\#3}$	88.7(2)	N(13)$^{\#4}$-Ni(4)-O(8)$^{\#4}$	86.74(19)
N(10)$^{\#3}$-Ni(3)-O(6)$^{\#3}$	91.3(2)	N(13)-Ni(4)-O(8)$^{\#4}$	93.26(19)
N(9)$^{\#3}$-Ni(3)-O(6)$^{\#3}$	88.6(2)	N(14)$^{\#4}$-Ni(4)-O(8)$^{\#4}$	93.3(2)
N(9)-Ni(3)-O(6)$^{\#3}$	91.4(2)	N(14)-Ni(4)-O(8)$^{\#4}$	86.7(2)
O(6)-Ni(3)-O(6)$^{\#3}$	180.0	O(8)-Ni(4)-O(8)$^{\#4}$	180.0

Symmetry transformations used to generate equivalent atoms:

#1 : -x,-y+1,-z #2 : -x,-y,-z+1 #3 : -x+1,-y,-z #4 : -x,-y+1,-z+1

Table S3. The bond lengths [Å] and angles[°] around nickel metal of **as-*flex*MOF(CN)-II**

Ni(1)-N(1)$^{\#1}$	2.041(5)	Ni(2)-N(5)$^{\#2}$	2.055(4)
Ni(1)-N(1)	2.041(5)	Ni(2)-N(5)	2.055(4)
Ni(1)-N(2)$^{\#1}$	2.053(4)	Ni(2)-N(6)	2.057(5)
Ni(1)-N(2)	2.053(4)	Ni(2)-N(6)$^{\#2}$	2.057(5)
Ni(1)-O(2)	2.133(3)	Ni(2)-O(4)	2.137(3)
Ni(1)-O(2)$^{\#1}$	2.133(3)	Ni(2)-O(4)$^{\#2}$	2.137(3)
Ni(3)-N(10)	2.026(4)	Ni(4)-N(13)	2.043(4)
Ni(3)-N(10)$^{\#3}$	2.026(4)	Ni(4)-N(13)$^{\#4}$	2.043(4)
Ni(3)-N(9)	2.083(8)	Ni(4)-N(14)$^{\#4}$	2.063(8)
Ni(3)-N(9)$^{\#3}$	2.083(8)	Ni(4)-N(14)	2.063(8)
Ni(3)-O(6)$^{\#3}$	2.104(4)	Ni(4)-O(8)$^{\#4}$	2.093(4)
Ni(3)-O(6)	2.104(4)	Ni(4)-O(8)	2.093(4)
N(1)$^{\#1}$-Ni(1)-N(1)	180.0	N(5)$^{\#2}$-Ni(2)-N(5)	180.0
N(1)$^{\#1}$-Ni(1)-N(2)$^{\#1}$	92.98(19)	N(5)$^{\#2}$-Ni(2)-N(6)	86.7(2)
N(1)-Ni(1)-N(2)$^{\#1}$	87.02(19)	N(5)-Ni(2)-N(6)	93.3(2)
N(1)$^{\#1}$-Ni(1)-N(2)	87.02(19)	N(5)$^{\#2}$-Ni(2)-N(6)$^{\#2}$	93.3(2)
N(1)-Ni(1)-N(2)	92.98(19)	N(5)-Ni(2)-N(6)$^{\#2}$	86.7(2)
N(2)$^{\#1}$-Ni(1)-N(2)	180.0	N(6)-Ni(2)-N(6)$^{\#2}$	180.0
N(1)$^{\#1}$-Ni(1)-O(2)	92.32(15)	N(5)$^{\#2}$-Ni(2)-O(4)	90.11(14)
N(1)-Ni(1)-O(2)	87.68(15)	N(5)-Ni(2)-O(4)	89.90(14)
N(2)$^{\#1}$-Ni(1)-O(2)	89.85(14)	N(6)-Ni(2)-O(4)	92.60(15)
N(2)-Ni(1)-O(2)	90.15(14)	N(6)$^{\#2}$-Ni(2)-O(4)	87.41(15)
N(1)$^{\#1}$-Ni(1)-O(2)$^{\#1}$	87.68(15)	N(5)$^{\#2}$-Ni(2)-O(4)$^{\#2}$	89.89(14)
N(1)-Ni(1)-O(2)$^{\#1}$	92.32(15)	N(5)-Ni(2)-O(4)$^{\#2}$	90.10(14)
N(2)$^{\#1}$-Ni(1)-O(2)$^{\#1}$	90.15(14)	N(6)-Ni(2)-O(4)$^{\#2}$	87.40(15)
N(2)-Ni(1)-O(2)$^{\#1}$	89.85(14)	N(6)$^{\#2}$-Ni(2)-O(4)$^{\#2}$	92.60(15)
O(2)-Ni(1)-O(2)$^{\#1}$	180.0	O(4)-Ni(2)-O(4)$^{\#2}$	180.0
N(10)-Ni(3)-N(10)$^{\#3}$	180.0	N(13)-Ni(4)-N(13)$^{\#4}$	180.0
N(10)-Ni(3)-N(9)	84.9(3)	N(13)-Ni(4)-N(14)$^{\#4}$	94.4(2)
N(10)$^{\#3}$-Ni(3)-N(9)	95.1(3)	N(13)$^{\#4}$-Ni(4)-N(14)$^{\#4}$	85.6(2)
N(10)-Ni(3)-N(9)$^{\#3}$	95.1(3)	N(13)-Ni(4)-N(14)	85.6(2)
N(10)$^{\#3}$-Ni(3)-N(9)$^{\#3}$	84.9(3)	N(13)$^{\#4}$-Ni(4)-N(14)	94.4(2)

N(9)-Ni(3)-N(9)$^{\#3}$	180.0	N(14)$^{\#4}$-Ni(4)-N(14)	180.0
N(10)-Ni(3)-O(6)$^{\#3}$	86.67(16)	N(13)-Ni(4)-O(8)$^{\#4}$	87.07(17)
N(10)$^{\#3}$-Ni(3)-O(6)$^{\#3}$	93.33(16)	N(13)$^{\#4}$-Ni(4)-O(8)$^{\#4}$	92.93(17)
N(9)-Ni(3)-O(6)$^{\#3}$	88.5(2)	N(14)$^{\#4}$-Ni(4)-O(8)$^{\#4}$	91.7(2)
N(9)$^{\#3}$-Ni(3)-O(6)$^{\#3}$	91.5(2)	N(14)-Ni(4)-O(8)$^{\#4}$	88.3(2)
N(10)-Ni(3)-O(6)	93.33(16)	N(13)-Ni(4)-O(8)	92.93(17)
N(10)$^{\#3}$-Ni(3)-O(6)	86.67(16)	N(13)$^{\#4}$-Ni(4)-O(8)	87.07(17)
N(9)-Ni(3)-O(6)	91.5(2)	N(14)$^{\#4}$-Ni(4)-O(8)	88.3(2)
N(9)$^{\#3}$-Ni(3)-O(6)	88.5(2)	N(14)-Ni(4)-O(8)	91.7(2)
O(6)$^{\#3}$-Ni(3)-O(6)	180.0	O(8)$^{\#4}$-Ni(4)-O(8)	180.0

Symmetry transformations used to generate equivalent atoms:

#1 : -x+1,-y+1,-z #2 : -x+1,-y,-z+1 #3 : -x,-y+1,-z+1 #4 : -x+1,-y,-z

Table S4. The bond lengths [Å] and angles[°] around nickel metal of ***d-flex*MOF(CN)-II**

Ni(1)-N(2)	2.024(5)	Ni(2)-N(5)$^{\#2}$	2.038(5)
Ni(1)-N(2)$^{\#1}$	2.024(5)	Ni(2)-N(5)	2.038(5)
Ni(1)-N(1)	2.054(5)	Ni(2)-N(6)	2.074(5)
Ni(1)-N(1)$^{\#1}$	2.054(5)	Ni(2)-N(6)$^{\#2}$	2.074(5)
Ni(1)-O(2)	2.073(4)	Ni(2)-O(4)$^{\#2}$	2.142(4)
Ni(1)-O(2)$^{\#1}$	2.073(4)	Ni(2)-O(4)	2.142(4)
Ni(3)-N(10)	2.039(5)	Ni(4)-N(13)	2.037(5)
Ni(3)-N(10)$^{\#3}$	2.039(5)	Ni(4)-N(13)$^{\#4}$	2.037(5)
Ni(3)-N(9)	2.065(5)	Ni(4)-N(14)$^{\#4}$	2.055(5)
Ni(3)-N(9)$^{\#3}$	2.065(5)	Ni(4)-N(14)	2.055(5)
Ni(3)-O(6)	2.070(4)	Ni(4)-O(8)	2.132(4)
Ni(3)-O(6)$^{\#3}$	2.070(4)	Ni(4)-O(8)$^{\#4}$	2.132(4)
N(2)-Ni(1)-N(2)$^{\#1}$	180.0	N(5)$^{\#2}$-Ni(2)-N(5)	180.0
N(2)-Ni(1)-N(1)	85.13(19)	N(5)$^{\#2}$-Ni(2)-N(6)	85.30(19)
N(2)$^{\#1}$-Ni(1)-N(1)	94.87(19)	N(5)-Ni(2)-N(6)	94.70(19)
N(2)-Ni(1)-N(1)$^{\#1}$	94.87(19)	N(5)$^{\#2}$-Ni(2)-N(6)$^{\#2}$	94.70(19)
N(2)$^{\#1}$-Ni(1)-N(1)$^{\#1}$	85.13(19)	N(5)-Ni(2)-N(6)$^{\#2}$	85.30(19)
N(1)-Ni(1)-N(1)$^{\#1}$	180.0	N(6)-Ni(2)-N(6)$^{\#2}$	180.00(12)
N(2)-Ni(1)-O(2)	89.53(19)	N(5)$^{\#2}$-Ni(2)-O(4)$^{\#2}$	87.16(16)
N(2)$^{\#1}$-Ni(1)-O(2)	90.47(19)	N(5)-Ni(2)-O(4)$^{\#2}$	92.84(16)
N(1)-Ni(1)-O(2)	91.52(17)	N(6)-Ni(2)-O(4)$^{\#2}$	90.32(16)
N(1)$^{\#1}$-Ni(1)-O(2)	88.48(17)	N(6)$^{\#2}$-Ni(2)-O(4)$^{\#2}$	89.68(16)
N(2)-Ni(1)-O(2)$^{\#1}$	90.47(19)	N(5)$^{\#2}$-Ni(2)-O(4)	92.84(16)
N(2)$^{\#1}$-Ni(1)-O(2)$^{\#1}$	89.53(19)	N(5)-Ni(2)-O(4)	87.16(16)
N(1)-Ni(1)-O(2)$^{\#1}$	88.48(17)	N(6)-Ni(2)-O(4)	89.68(16)
N(1)$^{\#1}$-Ni(1)-O(2)$^{\#1}$	91.52(17)	N(6)$^{\#2}$-Ni(2)-O(4)	90.32(16)
O(2)-Ni(1)-O(2)$^{\#1}$	180.0(2)	O(4)$^{\#2}$-Ni(2)-O(4)	180.0
N(10)-Ni(3)-N(10)$^{\#3}$	180.0(3)	N(13)-Ni(4)-N(13)$^{\#4}$	180.0(2)
N(10)-Ni(3)-N(9)	95.6(2)	N(13)-Ni(4)-N(14)$^{\#4}$	95.2(2)
N(10)$^{\#3}$-Ni(3)-N(9)	84.4(2)	N(13)$^{\#4}$-Ni(4)-N(14)$^{\#4}$	84.8(2)
N(10)-Ni(3)-N(9)$^{\#3}$	84.4(2)	N(13)-Ni(4)-N(14)	84.8(2)
N(10)$^{\#3}$-Ni(3)-N(9)$^{\#3}$	95.6(2)	N(13)$^{\#4}$-Ni(4)-N(14)	95.2(2)

N(9)-Ni(3)-N(9)$^{\#3}$	180.0	N(14)$^{\#4}$-Ni(4)-N(14)	180.0
N(10)-Ni(3)-O(6)	90.22(18)	N(13)-Ni(4)-O(8)	86.71(18)
N(10)$^{\#3}$-Ni(3)-O(6)	89.78(18)	N(13)$^{\#4}$-Ni(4)-O(8)	93.29(18)
N(9)-Ni(3)-O(6)	92.76(16)	N(14)$^{\#4}$-Ni(4)-O(8)	91.23(17)
N(9)$^{\#3}$-Ni(3)-O(6)	87.24(16)	N(14)-Ni(4)-O(8)	88.77(17)
N(10)-Ni(3)-O(6)$^{\#3}$	89.78(18)	N(13)-Ni(4)-O(8)$^{\#4}$	93.30(18)
N(10)$^{\#3}$-Ni(3)-O(6)$^{\#3}$	90.22(18)	N(13)$^{\#4}$-Ni(4)-O(8)$^{\#4}$	86.71(18)
N(9)-Ni(3)-O(6)$^{\#3}$	87.24(16)	N(14)$^{\#4}$-Ni(4)-O(8)$^{\#4}$	88.77(17)
N(9)$^{\#3}$-Ni(3)-O(6)$^{\#3}$	92.76(16)	N(14)-Ni(4)-O(8)$^{\#4}$	91.23(17)
O(6)-Ni(3)-O(6)$^{\#3}$	180.0	O(8)-Ni(4)-O(8)$^{\#4}$	180.00(12)

Symmetry transformations used to generate equivalent atoms:

#1 : -x+1,-y,-z+1 #2 : -x,-y+1,-z+1 #3 : -x+1,-y,-z+2 #4 : -x+1,-y+1,-z+2

Table S5. The bond lengths [Å] and angles[°] around nickel metal of ***as-flex*MOF(CH$_2$)**

O(1)-Ni(1)	2.112(3)	O(7)-Ni(2)	2.075(3)
Ni(1)-N(1)	2.045(4)	Ni(2)-N(8)$^{\#3}$	2.060(4)
Ni(1)-N(4)	2.049(4)	Ni(2)-N(8)	2.060(4)
Ni(1)-N(2)	2.053(4)	Ni(2)-N(7)$^{\#3}$	2.064(5)
Ni(1)-N(3)	2.064(4)	Ni(2)-N(7)	2.065(5)
Ni(1)-O(5)$^{\#2}$	2.121(3)	Ni(2)-O(7)$^{\#3}$	2.075(3)
O(4)-Ni(3)	2.105(3)		
Ni(3)-N(11)$^{\#4}$	2.041(4)		
Ni(3)-N(11)	2.041(4)		
Ni(3)-N(10)	2.048(5)		
Ni(3)-N(10)$^{\#4}$	2.048(5)		
Ni(3)-O(4)$^{\#4}$	2.105(3)		
N(1)-Ni(1)-N(4)	93.10(17)	N(8)$^{\#3}$-Ni(2)-N(8)	180.0
N(1)-Ni(1)-N(2)	86.91(17)	N(8)$^{\#3}$-Ni(2)-N(7)$^{\#3}$	91.81(19)
N(4)-Ni(1)-N(2)	179.84(14)	N(8)-Ni(2)-N(7)$^{\#3}$	88.19(19)
N(1)-Ni(1)-N(3)	178.98(16)	N(8)$^{\#3}$-Ni(2)-N(7)	88.19(19)
N(4)-Ni(1)-N(3)	85.91(17)	N(8)-Ni(2)-N(7)	91.81(19)
N(2)-Ni(1)-N(3)	94.08(17)	N(7)$^{\#3}$-Ni(2)-N(7)	180.0
N(1)-Ni(1)-O(1)	93.43(14)	N(8)$^{\#3}$-Ni(2)-O(7)	94.85(15)
N(4)-Ni(1)-O(1)	90.49(16)	N(8)-Ni(2)-O(7)	85.15(15)
N(2)-Ni(1)-O(1)	89.67(15)	N(7)$^{\#3}$-Ni(2)-O(7)	87.11(19)
N(3)-Ni(1)-O(1)	86.33(14)	N(7)-Ni(2)-O(7)	92.89(19)
N(1)-Ni(1)-O(5)$^{\#2}$	86.64(15)	N(8)$^{\#3}$-Ni(2)-O(7)$^{\#3}$	85.15(15)
N(4)-Ni(1)-O(5)$^{\#2}$	90.24(15)	N(8)-Ni(2)-O(7)$^{\#3}$	94.85(15)
N(2)-Ni(1)-O(5)$^{\#2}$	89.60(15)	N(7)$^{\#3}$-Ni(2)-O(7)$^{\#3}$	92.89(19)
N(3)-Ni(1)-O(5)$^{\#2}$	93.62(14)	N(7)-Ni(2)-O(7)$^{\#3}$	87.11(19)
O(1)-Ni(1)-O(5)$^{\#2}$	179.26(12)	O(7)-Ni(2)-O(7)$^{\#3}$	180.0(2)
N(11)$^{\#4}$-Ni(3)-N(11)	180.0		
N(11)$^{\#4}$-Ni(3)-N(10)	87.77(19)		
N(11)-Ni(3)-N(10)	92.23(19)		
N(11)$^{\#4}$-Ni(3)-N(10)$^{\#4}$	92.24(19)		
N(11)-Ni(3)-N(10)$^{\#4}$	87.76(19)		

N(10)-Ni(3)-N(10)$^{\#4}$	180.0
N(11)$^{\#4}$-Ni(3)-O(4)	86.96(16)
N(11)-Ni(3)-O(4)	93.04(15)
N(10)-Ni(3)-O(4)	88.9(2)
N(10)$^{\#4}$-Ni(3)-O(4)	91.1(2)
N(11)$^{\#4}$-Ni(3)-O(4)$^{\#4}$	93.04(15)
N(11)-Ni(3)-O(4)$^{\#4}$	86.96(15)
N(10)-Ni(3)-O(4)$^{\#4}$	91.1(2)
N(10)$^{\#4}$-Ni(3)-O(4)$^{\#4}$	88.9(2)
O(4)-Ni(3)-O(4)$^{\#4}$	180.0

Symmetry transformations used to generate equivalent atoms:

#1 : x+1/2,-y+1/2,z+1/2 #2 : x-1/2,-y+1/2,z-1/2 #3 : -x+2,-y,-z+1 #4 : -x+2,-y,-z+2

Table S6. The bond lengths [Å] and angles[°] around nickel metal of ***d-flex*MOF(CH$_2$)**

Ni(1)-N(2)$^{\#1}$	2.062(7)	Ni(2)-N(5)	2.012(8)
Ni(1)-N(2)	2.063(7)	Ni(2)-N(5)$^{\#2}$	2.012(8)
Ni(1)-N(1)	2.063(8)	Ni(2)-N(4)	2.080(8)
Ni(1)-N(1)$^{\#1}$	2.063(8)	Ni(2)-N(4)$^{\#2}$	2.080(8)
Ni(1)-O(2)	2.109(6)	Ni(2)-O(4)	2.167(5)
Ni(1)-O(2)$^{\#1}$	2.109(6)	Ni(2)-O(4)$^{\#2}$	2.167(5)
Ni(3)-N(7)$^{\#3}$	2.041(8)	Ni(4)-N(11)	2.024(8)
Ni(3)-N(7)	2.041(8)	Ni(4)-N(11)$^{\#4}$	2.024(8)
Ni(3)-N(8)	2.057(9)	Ni(4)-N(10)$^{\#4}$	2.053(11)
Ni(3)-N(8)$^{\#3}$	2.057(9)	Ni(4)-N(10)	2.053(11)
Ni(3)-O(6)	2.169(6)	Ni(4)-O(8)	2.136(6)
Ni(3)-O(6)$^{\#3}$	2.169(6)	Ni(4)-O(8)$^{\#4}$	2.136(6)
N(2)$^{\#1}$-Ni(1)-N(2)	180.0	N(5)-Ni(2)-N(5)$^{\#2}$	180.0
N(2)$^{\#1}$-Ni(1)-N(1)	96.0(3)	N(5)-Ni(2)-N(4)	85.6(3)
N(2)-Ni(1)-N(1)	84.0(3)	N(5)$^{\#2}$-Ni(2)-N(4)	94.4(3)
N(2)$^{\#1}$-Ni(1)-N(1)$^{\#1}$	84.0(3)	N(5)-Ni(2)-N(4)$^{\#2}$	94.4(3)
N(2)-Ni(1)-N(1)$^{\#1}$	96.0(3)	N(5)$^{\#2}$-Ni(2)-N(4)$^{\#2}$	85.6(3)
N(1)-Ni(1)-N(1)$^{\#1}$	180.0	N(4)-Ni(2)-N(4)$^{\#2}$	180.00(14)
N(2)$^{\#1}$-Ni(1)-O(2)	85.7(3)	N(5)-Ni(2)-O(4)	87.1(3)
N(2)-Ni(1)-O(2)	94.3(3)	N(5)$^{\#2}$-Ni(2)-O(4)	92.9(3)
N(1)-Ni(1)-O(2)	92.1(3)	N(4)-Ni(2)-O(4)	85.5(3)
N(1)$^{\#1}$-Ni(1)-O(2)	87.9(3)	N(4)$^{\#2}$-Ni(2)-O(4)	94.5(3)
N(2)$^{\#1}$-Ni(1)-O(2)$^{\#1}$	94.3(3)	N(5)-Ni(2)-O(4)$^{\#2}$	92.9(3)
N(2)-Ni(1)-O(2)$^{\#1}$	85.7(3)	N(5)$^{\#2}$-Ni(2)-O(4)$^{\#2}$	87.1(3)
N(1)-Ni(1)-O(2)$^{\#1}$	87.9(3)	N(4)-Ni(2)-O(4)$^{\#2}$	94.5(3)
N(1)$^{\#1}$-Ni(1)-O(2)$^{\#1}$	92.1(3)	N(4)$^{\#2}$-Ni(2)-O(4)$^{\#2}$	85.5(3)
O(2)-Ni(1)-O(2)$^{\#1}$	180.0	O(4)-Ni(2)-O(4)$^{\#2}$	180.0(3)
N(7)$^{\#3}$-Ni(3)-N(7)	180.00(18)	N(11)-Ni(4)-N(11)$^{\#4}$	180.0(6)
N(7)$^{\#3}$-Ni(3)-N(8)	86.3(3)	N(11)-Ni(4)-N(10)$^{\#4}$	92.3(4)
N(7)-Ni(3)-N(8)	93.7(3)	N(11)$^{\#4}$-Ni(4)-N(10)$^{\#4}$	87.7(4)
N(7)$^{\#3}$-Ni(3)-N(8)$^{\#3}$	93.7(3)	N(11)-Ni(4)-N(10)	87.7(4)
N(7)-Ni(3)-N(8)$^{\#3}$	86.3(3)	N(11)$^{\#4}$-Ni(4)-N(10)	92.3(4)

N(8)-Ni(3)-N(8)$^{\#3}$	180.0	N(10)$^{\#4}$-Ni(4)-N(10)	180.0
N(7)$^{\#3}$-Ni(3)-O(6)	87.2(3)	N(11)-Ni(4)-O(8)	85.1(3)
N(7)-Ni(3)-O(6)	92.8(3)	N(11)$^{\#4}$-Ni(4)-O(8)	94.9(3)
N(8)-Ni(3)-O(6)	89.0(3)	N(10)$^{\#4}$-Ni(4)-O(8)	92.3(3)
N(8)$^{\#3}$-Ni(3)-O(6)	91.0(3)	N(10)-Ni(4)-O(8)	87.7(3)
N(7)$^{\#3}$-Ni(3)-O(6)$^{\#3}$	92.8(3)	N(11)-Ni(4)-O(8)$^{\#4}$	94.9(3)
N(7)-Ni(3)-O(6)$^{\#3}$	87.2(3)	N(11)$^{\#4}$-Ni(4)-O(8)$^{\#4}$	85.1(3)
N(8)-Ni(3)-O(6)$^{\#3}$	91.0(3)	N(10)$^{\#4}$-Ni(4)-O(8)$^{\#4}$	87.7(3)
N(8)$^{\#3}$-Ni(3)-O(6)$^{\#3}$	89.0(3)	N(10)-Ni(4)-O(8)$^{\#4}$	92.3(3)
O(6)-Ni(3)-O(6)$^{\#3}$	180.0	O(8)-Ni(4)-O(8)$^{\#4}$	180.0

Symmetry transformations used to generate equivalent atoms:

#1 : -x+1,-y+1,-z+2 #2 : -x,-y+2,-z+2 #3 : -x+1,-y+1,-z+1 #4 : -x+1,-y+2,-z+1

Table S7. The bond lengths [Å] and angles[°] around nickel metal of ***as-flex*MOF(OH)**

Ni(1)-N(2)	2.068(6)	Ni(2)-N(5)$^{\#2}$	2.052(5)
Ni(1)-N(2)$^{\#1}$	2.068(6)	Ni(2)-N(5)	2.052(5)
Ni(1)-N(1)$^{\#1}$	2.077(6)	Ni(2)-N(4)	2.080(6)
Ni(1)-N(1)	2.077(6)	Ni(2)-N(4)$^{\#2}$	2.080(6)
Ni(1)-O(2)	2.097(4)	Ni(2)-O(4)	2.113(5)
Ni(1)-O(2)$^{\#1}$	2.097(4)	Ni(2)-O(4)$^{\#2}$	2.113(5)
Ni(3)-N(8)$^{\#3}$	2.026(6)	Ni(4)-N(11)	2.030(7)
Ni(3)-N(8)	2.026(6)	Ni(4)-N(11)$^{\#4}$	2.030(7)
Ni(3)-N(7)	2.047(7)	Ni(4)-N(10)	2.034(7)
Ni(3)-N(7)$^{\#3}$	2.047(7)	Ni(4)-N(10)$^{\#4}$	2.034(7)
Ni(3)-O(6)$^{\#3}$	2.132(5)	Ni(4)-O(8)$^{\#4}$	2.107(5)
Ni(3)-O(6)	2.132(5)	Ni(4)-O(8)	2.107(5)
N(2)-Ni(1)-N(2)$^{\#1}$	180.0	N(5)$^{\#2}$-Ni(2)-N(5)	180.0
N(2)-Ni(1)-N(1)$^{\#1}$	94.7(2)	N(5)$^{\#2}$-Ni(2)-N(4)	93.1(2)
N(2)$^{\#1}$-Ni(1)-N(1)$^{\#1}$	85.3(2)	N(5)-Ni(2)-N(4)	86.9(2)
N(2)-Ni(1)-N(1)	85.3(2)	N(5)$^{\#2}$-Ni(2)-N(4)$^{\#2}$	86.9(2)
N(2)$^{\#1}$-Ni(1)-N(1)	94.7(2)	N(5)-Ni(2)-N(4)$^{\#2}$	93.1(2)
N(1)$^{\#1}$-Ni(1)-N(1)	180.0(7)	N(4)-Ni(2)-N(4)$^{\#2}$	180.0
N(2)-Ni(1)-O(2)	88.3(2)	N(5)$^{\#2}$-Ni(2)-O(4)	91.9(2)
N(2)$^{\#1}$-Ni(1)-O(2)	91.7(2)	N(5)-Ni(2)-O(4)	88.1(2)
N(1)$^{\#1}$-Ni(1)-O(2)	92.6(2)	N(4)-Ni(2)-O(4)	87.4(2)
N(1)-Ni(1)-O(2)	87.4(2)	N(4)$^{\#2}$-Ni(2)-O(4)	92.6(2)
N(2)-Ni(1)-O(2)$^{\#1}$	91.7(2)	N(5)$^{\#2}$-Ni(2)-O(4)$^{\#2}$	88.1(2)
N(2)$^{\#1}$-Ni(1)-O(2)$^{\#1}$	88.3(2)	N(5)-Ni(2)-O(4)$^{\#2}$	91.9(2)
N(1)$^{\#1}$-Ni(1)-O(2)$^{\#1}$	87.4(2)	N(4)-Ni(2)-O(4)$^{\#2}$	92.6(2)
N(1)-Ni(1)-O(2)$^{\#1}$	92.6(2)	N(4)$^{\#2}$-Ni(2)-O(4)$^{\#2}$	87.4(2)
O(2)-Ni(1)-O(2)$^{\#1}$	180.0(3)	O(4)-Ni(2)-O(4)$^{\#2}$	180.0
N(8)$^{\#3}$-Ni(3)-N(8)	180.0	N(11)-Ni(4)-N(11)$^{\#4}$	180.0
N(8)$^{\#3}$-Ni(3)-N(7)	94.6(2)	N(11)-Ni(4)-N(10)	94.9(3)
N(8)-Ni(3)-N(7)	85.4(2)	N(11)$^{\#4}$-Ni(4)-N(10)	85.1(3)
N(8)$^{\#3}$-Ni(3)-N(7)$^{\#3}$	85.4(2)	N(11)-Ni(4)-N(10)$^{\#4}$	85.1(3)
N(8)-Ni(3)-N(7)$^{\#3}$	94.6(2)	N(11)$^{\#4}$-Ni(4)-N(10)$^{\#4}$	94.9(3)

N(7)-Ni(3)-N(7)$^{\#3}$	180.0(4)	N(10)-Ni(4)-N(10)$^{\#4}$	180.0
N(8)$^{\#3}$-Ni(3)-O(6)$^{\#3}$	88.9(2)	N(11)-Ni(4)-O(8)$^{\#4}$	87.5(3)
N(8)-Ni(3)-O(6)$^{\#3}$	91.1(2)	N(11)$^{\#4}$-Ni(4)-O(8)$^{\#4}$	92.5(3)
N(7)-Ni(3)-O(6)$^{\#3}$	92.4(2)	N(10)-Ni(4)-O(8)$^{\#4}$	93.5(2)
N(7)$^{\#3}$-Ni(3)-O(6)$^{\#3}$	87.6(2)	N(10)$^{\#4}$-Ni(4)-O(8)$^{\#4}$	86.5(2)
N(8)$^{\#3}$-Ni(3)-O(6)	91.1(2)	N(11)-Ni(4)-O(8)	92.5(3)
N(8)-Ni(3)-O(6)	88.9(2)	N(11)$^{\#4}$-Ni(4)-O(8)	87.5(3)
N(7)-Ni(3)-O(6)	87.6(2)	N(10)-Ni(4)-O(8)	86.5(2)
N(7)$^{\#3}$-Ni(3)-O(6)	92.4(2)	N(10)$^{\#4}$-Ni(4)-O(8)	93.5(2)
O(6)$^{\#3}$-Ni(3)-O(6)	180.0	O(8)$^{\#4}$-Ni(4)-O(8)	180.0(3)

Symmetry transformations used to generate equivalent atoms:

#1 : -x+1,-y,-z+2 #2 : -x+1,-y+1,-z+1 #3 : -x+1,-y,-z+1 #4 : -x,-y+1,-z+2

Table S8. The bond lengths [Å] and angles[°] around nickel metal of ***d-flex*MOF(OH)**

Ni(1)-N(2)$^{\#1}$	2.046(5)	Ni(2)-N(5)	2.024(5)
Ni(1)-N(2)	2.046(5)	Ni(2)-N(5)$^{\#2}$	2.024(5)
Ni(1)-N(1)$^{\#1}$	2.047(6)	Ni(2)-N(4)	2.042(6)
Ni(1)-N(1)	2.047(6)	Ni(2)-N(4)$^{\#2}$	2.042(6)
Ni(1)-O(2)	2.125(4)	Ni(2)-O(4)$^{\#2}$	2.167(4)
Ni(1)-O(2)$^{\#1}$	2.125(4)	Ni(2)-O(4)	2.167(4)
Ni(3)-N(8)$^{\#3}$	2.054(6)	Ni(4)-N(10)$^{\#4}$	2.027(6)
Ni(3)-N(8)	2.054(6)	Ni(4)-N(10)	2.027(6)
Ni(3)-N(7)$^{\#3}$	2.046(5)	Ni(4)-N(11)	2.063(6)
Ni(3)-N(7)	2.046(5)	Ni(4)-N(11)$^{\#4}$	2.063(6)
Ni(3)-O(6)$^{\#3}$	2.163(4)	Ni(4)-O(8)$^{\#4}$	2.141(4)
Ni(3)-O(6)	2.163(4)	Ni(4)-O(8)	2.141(4)
N(2)$^{\#1}$-Ni(1)-N(2)	180.0	N(5)-Ni(2)-N(5)$^{\#2}$	180.0
N(2)$^{\#1}$-Ni(1)-N(1)$^{\#1}$	92.6(2)	N(5)-Ni(2)-N(4)	85.5(2)
N(2)-Ni(1)-N(1)$^{\#1}$	87.4(2)	N(5)$^{\#2}$-Ni(2)-N(4)	94.5(2)
N(2)$^{\#1}$-Ni(1)-N(1)	87.4(2)	N(5)-Ni(2)-N(4)$^{\#2}$	94.5(2)
N(2)-Ni(1)-N(1)	92.6(2)	N(5)$^{\#2}$-Ni(2)-N(4)$^{\#2}$	85.5(2)
N(1)$^{\#1}$-Ni(1)-N(1)	180.0	N(4)-Ni(2)-N(4)$^{\#2}$	180.0
N(2)$^{\#1}$-Ni(1)-O(2)	87.53(19)	N(5)-Ni(2)-O(4)$^{\#2}$	87.99(19)
N(2)-Ni(1)-O(2)	92.47(19)	N(5)$^{\#2}$-Ni(2)-O(4)$^{\#2}$	92.01(19)
N(1)$^{\#1}$-Ni(1)-O(2)	93.78(19)	N(4)-Ni(2)-O(4)$^{\#2}$	87.4(2)
N(1)-Ni(1)-O(2)	86.22(19)	N(4)$^{\#2}$-Ni(2)-O(4)$^{\#2}$	92.6(2)
N(2)$^{\#1}$-Ni(1)-O(2)$^{\#1}$	92.47(19)	N(5)-Ni(2)-O(4)	92.01(19)
N(2)-Ni(1)-O(2)$^{\#1}$	87.53(19)	N(5)$^{\#2}$-Ni(2)-O(4)	87.99(19)
N(1)$^{\#1}$-Ni(1)-O(2)$^{\#1}$	86.22(19)	N(4)-Ni(2)-O(4)	92.6(2)
N(1)-Ni(1)-O(2)$^{\#1}$	93.78(19)	N(4)$^{\#2}$-Ni(2)-O(4)	87.4(2)
O(2)-Ni(1)-O(2)$^{\#1}$	180.0	O(4)$^{\#2}$-Ni(2)-O(4)	180.0
N(8)$^{\#3}$-Ni(3)-N(8)	180.0	N(10)$^{\#4}$-Ni(4)-N(10)	180.0
N(8)$^{\#3}$-Ni(3)-N(7)$^{\#3}$	94.4(2)	N(10)$^{\#4}$-Ni(4)-N(11)	86.1(2)
N(8)-Ni(3)-N(7)$^{\#3}$	85.6(2)	N(10)-Ni(4)-N(11)	93.9(2)
N(8)$^{\#3}$-Ni(3)-N(7)	85.6(2)	N(10)$^{\#4}$-Ni(4)-N(11)$^{\#4}$	93.9(2)
N(8)-Ni(3)-N(7)	94.4(2)	N(10)-Ni(4)-N(11)$^{\#4}$	86.1(2)

N(7)$^{\#3}$-Ni(3)-N(7)	180.0	N(11)-Ni(4)-N(11)$^{\#4}$	180.0
N(8)$^{\#3}$-Ni(3)-O(6)$^{\#3}$	91.6(2)	N(10)$^{\#4}$-Ni(4)-O(8)$^{\#4}$	92.2(2)
N(8)-Ni(3)-O(6)$^{\#3}$	88.4(2)	N(10)-Ni(4)-O(8)$^{\#4}$	87.8(2)
N(7)$^{\#3}$-Ni(3)-O(6)$^{\#3}$	86.23(19)	N(11)-Ni(4)-O(8)$^{\#4}$	92.3(2)
N(7)-Ni(3)-O(6)$^{\#3}$	93.77(19)	N(11)$^{\#4}$-Ni(4)-O(8)$^{\#4}$	87.7(2)
N(8)$^{\#3}$-Ni(3)-O(6)	88.4(2)	N(10)$^{\#4}$-Ni(4)-O(8)	87.9(2)
N(8)-Ni(3)-O(6)	91.6(2)	N(10)-Ni(4)-O(8)	92.2(2)
N(7)$^{\#3}$-Ni(3)-O(6)	93.77(19)	N(11)-Ni(4)-O(8)	87.7(2)
N(7)-Ni(3)-O(6)	86.23(19)	N(11)$^{\#4}$-Ni(4)-O(8)	92.3(2)
O(6)$^{\#3}$-Ni(3)-O(6)	180.0(2)	O(8)$^{\#4}$-Ni(4)-O(8)	180.0

Symmetry transformations used to generate equivalent atoms:

#1 : -x+1,-y+2,-z #2 : -x+2,-y+2,-z+1 #3 : -x+1,-y+1,-z #4 : -x+1,-y+1,-z+1